Title

Robust, fully-automated assessment of cerebral perivascular spaces and white matter lesions: a multicentre MRI longitudinal study of their evolution and association with risk of dementia and accelerated brain atrophy

Authors

Barisano, Giuseppe
Iv, Michael
Choupan, Jeiran
et al.

Publication Date

2025

DOI

10.1016/j.ebiom.2024.105523

Peer reviewed

Robust, fully-automated assessment of cerebral perivascular spaces and white matter lesions: a multicentre MRI longitudinal study of their evolution and association with risk of dementia and accelerated brain atrophy

Giuseppe Barisano,[a,*] Michael Iv,[b] Jeiran Choupan,[c,d] and Melanie Hayden-Gephart,[a] on behalf of the Alzheimer's Disease Neuroimaging Initiative[e]

[a]Department of Neurosurgery, Stanford University, Stanford, CA, USA
[b]Department of Radiology, Stanford University, Stanford, CA, USA
[c]Laboratory of Neuro Imaging, University of Southern California, Los Angeles, CA, USA
[d]NeuroScope Inc., New York, NY, USA

eBioMedicine
2025;111: 105523
Published Online xxx
https://doi.org/10.1016/j.ebiom.2024.105523

Summary

Background Perivascular spaces (PVS) on brain MRI are surrogates for small parenchymal blood vessels and their perivascular compartment, and may relate to brain health. However, it is unknown whether PVS can predict dementia risk and brain atrophy trajectories in participants without dementia, as longitudinal studies on PVS are scarce and current methods for PVS assessment lack robustness and inter-scanner reproducibility.

Methods We developed a robust algorithm to automatically assess PVS count and size on clinical MRI, and investigated 1) their relationship with dementia risk and brain atrophy in participants without dementia, 2) their longitudinal evolution, and 3) their potential use as a screening tool in simulated clinical trials. We analysed 46,478 clinical measurements of cognitive functioning and 20,845 brain MRI scans from 10,004 participants (71.1 ± 9.7 years-old, 56.6% women) from three publicly available observational studies on ageing and dementia (the Alzheimer's Disease Neuroimaging Initiative, the National Alzheimer's Coordinating Centre database, and the Open Access Series of Imaging Studies). Clinical and MRI data collected between 2004 and 2022 were analysed with consistent methods, controlling for confounding factors, and combined using mixed-effects models.

Findings Our fully-automated method for PVS assessment showed excellent inter-scanner reproducibility (intraclass correlation coefficients >0.8). Fewer PVS and larger PVS diameter at baseline predicted higher dementia risk and accelerated brain atrophy. Longitudinal trajectories of PVS markers differed significantly in participants without dementia who converted to dementia compared with non-converters. In simulated placebo-controlled trials for treatments targeting cognitive decline, screening out participants at low risk of dementia based on our PVS markers enhanced the power of the trial independently of Alzheimer's disease biomarkers.

Interpretation These robust cerebrovascular markers predict dementia risk and brain atrophy and may improve risk-stratification of patients, potentially reducing cost and increasing throughput of clinical trials to combat dementia.

Funding US National Institutes of Health.

Keywords: Perivascular spaces; White matter lesions; Small vessel disease; Dementia; Alzheimer's disease; Glymphatic system

Introduction

Cerebral small vessel disease, the most common vascular disease affecting the blood vessels within the brain parenchyma, is considered a significant and potentially reversible contributor to cognitive decline and dementia.[1,2] *Ex vivo* studies have shown an independent association of cerebral small vessel neuropathology with cognitive function and many subtypes of

*Corresponding author. Department of Neurosurgery, Stanford University, 1201 Welch Rd., Stanford, CA 94305, USA.
E-mail address: barisano@stanford.edu (G. Barisano).
[e]Members of the Alzheimer's Disease Neuroimaging Initiative study group are listed in the Acknowledgements section.

Research in context

Evidence before this study

We searched PubMed, Google Scholar, and Web of Science for articles published up to April, 2024, with the terms ("Perivascular spaces" OR "PVS" OR "EPVS" OR "Virchow-Robin spaces" OR "VRS") AND ("Dementia" OR "Alzheimer" OR "Cognitive impairment") AND "longitudinal" without any language restriction. This search yielded 51 results. Abstracts and titles were reviewed. Only five research articles (two of which were also included in three meta-analyses) reported data on perivascular spaces (PVS) and incident dementia risk. The results are conflicting and the relationship between PVS and dementia risk remains unclear. Importantly, all these studies performed only a manual visual assessment of PVS, which has critical limitations related to inter- and intra-rater variability, low sensitivity, and lack of granularity. Moreover, the models in these studies inconsistently controlled for confounding factors and did not include Alzheimer's biomarkers amyloid-β or tau. None of these studies performed a quantitative assessment of PVS. Neither the relationship between PVS and brain atrophy trajectories nor the longitudinal evolution of PVS were explored. Our search therefore suggested that little is known about the longitudinal evolution of PVS and their relation to dementia risk and brain atrophy.

The increasing evidence that vascular pathology contributes to cognitive dysfunction highlights the critical need for the development of robust MRI markers of cerebral small vessel disease and PVS that could be used in hospitals, research, and clinical trials to disentangle their contributions to cognitive impairment and dementia. We searched PubMed, Google Scholar, and Web of Science for articles published up to April, 2024, with the terms ("Perivascular spaces" OR "PVS" OR "EPVS" OR "Virchow-Robin spaces" OR "VRS") AND ("Comput*" OR "Segmentation" OR "Quantif*" OR "Algorithm*" OR "Automat*" OR "Semi-auto*" OR "Semiauto*"). We identified 45 articles describing methods for the segmentation and/or quantification of vascular and perivascular structural properties. None of these methods could be considered fully-automated, as they include steps requiring a human intervention (e.g., selection of thresholds for filtering techniques) and/or human-based training datasets for artificial intelligence algorithms. Importantly, the inter-scanner reproducibility of these methods was also not described or weak.

Added value of this study

Here we present a fully-automated algorithm which segments PVS from clinical T1-weighted images and provides robust estimates of PVS count and size with excellent inter-scanner reproducibility and test-retest repeatability (intraclass correlation coefficients > 0.8). These characteristics allowed us to employ this technique to quantitatively assess PVS on 20,845 brain MRI scans of 10,004 participants whose data were pooled from three publicly available studies performed in the United States and Canada. Our results show that fewer PVS and larger PVS diameter at baseline predicted higher dementia risk and accelerated brain atrophy. Longitudinal trajectories of PVS markers differed significantly in participants without dementia who converted to dementia compared with non-converters. These results were independent of APOE genotype, vascular risk factors, and, for most cases, amyloid-β and tau status. Our data add important information to current knowledge of vascular contributions to dementia and brain atrophy. Moreover, we show that our PVS markers may enhance the power of clinical trials for treatments targeting cognitive decline and support risk-stratification of elderly participants without dementia independently of Alzheimer's disease biomarkers.

Implications of all the available evidence

The simplicity and efficiency of our algorithm in robustly and automatically assessing PVS on clinical MRI facilitate its easy implementation in hospitals, clinical trials, and even retrospectively for MRI data already acquired. The early identification of people at increased risk of dementia and accelerated brain atrophy according to our PVS markers has several clinically relevant implications, including: 1) enabling healthcare professionals to inform patients about their specific risk and to implement preventive measures and timely support; 2) enhancing the power of clinical trials targeting cognitive decline; 3) enhancing clinical trials targeting Alzheimer disease hallmark pathology (i.e., amyloid-β and/or tau) for a more homogenous cohort of preclinical Alzheimer disease by excluding participants with high-risk PVS markers; 4) opening new opportunities to robustly investigate perivascular spaces *in vivo* in a variety of neurological conditions and treatment paradigms, allowing to gain new insights on the physiology, pathophysiology, and treatments related to the human brain vasculature and glymphatics.

dementia.[3–7] Given the known association with dementia, it is important to identify robust radiographic markers of cerebral small vessel disease, to properly risk-stratify patients, monitor disease, and assess the impact of treatment.

In vivo evaluation of cerebral small vessel disease relies on magnetic resonance imaging (MRI) and includes different signs of brain parenchymal damage (e.g., white matter lesions, lacunes, subcortical infarcts, cerebral microbleeds, and enlargement of perivascular spaces).[8] Yet these MRI findings may not be detectable in the healthy population, are traditionally assessed with visual qualitative scales which have lower sensitivity compared with quantitative measures,[8,9] require specific MRI sequences, or are labour intensive to process.[1,2] Using the perivascular spaces (PVS) as detected on

MRI to non-invasively evaluate cerebral small vessel health requires only an unenhanced 3-dimensional T1-weighted images,[9] a nearly universal brain MRI sequence. Current techniques of PVS estimation[10–15] though suffer from user-dependency, and weak or unknown robustness and inter-scanner reproducibility.[1,9,16–18] These limitations prevent generalised, widespread use in the hospital, clinical trials, and multi-centre longitudinal studies. New, robust tools, therefore, are needed to investigate the temporality and nonspurious dose-response relationship between PVS (as a surrogate of cerebral small vessels) and dementia.

To meet this critical need, we developed and validated a fully automated approach to robustly assess PVS in the white matter (WM-PVS) and basal ganglia (BG-PVS) requiring as input only unenhanced 3-D T1-weighted images. Despite some possible limitations in PVS visual detection compared with T2-weighted images,[8] 3-D T1-weighted images are more commonly included in brain MRI protocols,[19] whereas 3-D T2-weighted images are less common in hospital and research settings, partly because they generally require longer acquisition times than T1-weighted images and some MRI scanners might not have a 3-D T2-weighted sequence implemented in their standard imaging protocols. Indeed, this was the case for the MRI data gathered in this study, which included 3-D T2-weighted images in less than 10% of the MRI sessions and only from one of the three assessed cohorts [Open Access Series of Imaging Studies (OASIS-3)]. Therefore, we considered the identification of PVS structural properties with clinical significance derived from 3-D T1-weighted images rather than T2-weighted images would be more widely applicable both in clinical and research settings.

We employed our method to investigate the following clinical questions which currently remain unsolved: the longitudinal evolution of PVS and the association of baseline PVS with the risk of developing dementia and with the brain atrophy trajectory in participants without dementia. We focused on two PVS properties: the total number of PVS (regardless of their enlargement status) on T1-weighted image (hereinafter referred to as PVS count), and PVS mean diameter. We also included in our analyses the (log-transformed) volume of white matter lesions (WML) in the periventricular area (P-WML) and deep white matter (D-WML), since they can similarly be measured on T1-weighted images and are considered closely related to PVS.[8]

Furthermore, given that the inclusion of participants with low risk of cognitive decline reduces the power of clinical trials evaluating a treatment effect on cognitive impairment,[20] we evaluated the potential benefit of our PVS markers as a screening tool to enrich for participants likely to develop dementia and compared their performance with that of standard WML and atrophy markers assessed on T1-weighted images. In summary, here we aim to investigate: 1) the relationship of our PVS markers with dementia risk and brain atrophy in participants without dementia, 2) their longitudinal evolution, and 3) their potential use as a screening tool in simulated clinical trials.

We hypothesised that: 1) our robust PVS markers may predict dementia risk and accelerated brain atrophy in an elderly population without dementia, 2) their longitudinal trajectories would be significantly different in participants without dementia who converted to dementia compared with those who did not convert, and 3) they could be used to increase the power of clinical trials for treatments targeting cognitive decline by enriching the sample size for participants more likely to experience cognitive dysfunction over time.

Methods

Study population

We combined data from three observational studies: the Alzheimer's Disease Neuroimaging Initiative (ADNI)[21] (MRI data downloaded on March 2023), the National Alzheimer's Coordinating Centre (NACC) database[22] (December 2022 data freeze), and the Open Access Series of Imaging Studies (OASIS-3)[23] (Data release 2.0, July 2022). Data were collected in the United States and Canada from 2004 to 2022. Enrolled participants include both cognitively unimpaired individuals and patients with cognitive impairment and dementia. All participants undergo standardised clinical and neuropsychological examination. In our analysis, "sex" indicates biological sex as was recorded in the clinical examination and "race" was reported by the participant as one or more of the following categories: "White", "Black", "American Indian", and "Asian".

We included in our analysis all participants who underwent 1) at least one clinical visit with cognitive assessment data available and 2) a brain MRI scan including an unenhanced 3-dimensional T1-weighted sequence within 12 months from the baseline clinical visit. In the analysis investigating the risk of dementia, and in the simulated clinical trials, only baseline participants without dementia with at least 1 follow-up clinical visit were included (definition of dementia is described in the following section). In the analysis of PVS and brain atrophy trajectories assessed with MRI, only baseline participants without dementia with at least 1 follow-up MRI scan were included (Fig. 1).

ADNI

ADNI is a longitudinal multicentre study conducted in the United States and Canada to develop clinical, imaging, genetic, and biochemical biomarkers for the early detection and tracking of Alzheimer's disease. ADNI began in 2004 and enrol participants with or without cognitive impairment between 55 and 90 years of age (inclusive) along with a study partner to provide an independent evaluation of functioning.[24] All participants

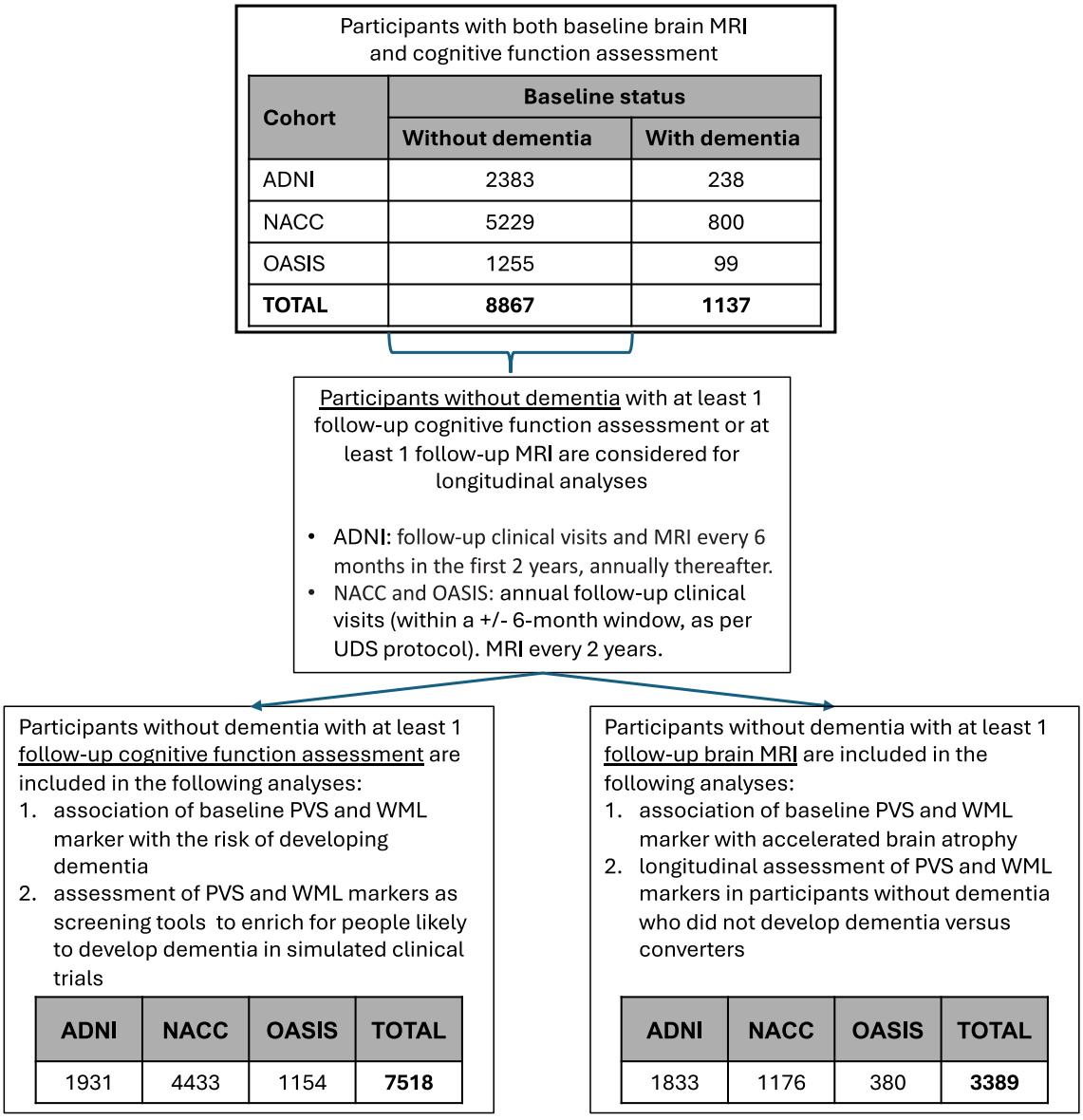

***Fig. 1:* Flowchart diagram depicting study design.** Further information about the participants clinical and demographic information can be found in Table 2 and Supplementary Tables S5 and S7.

could not have any medical contraindications to MRI, could not be enrolled in other trials or studies concurrently, and could not take any medication that could affect cognitive function.[24] All participants had to have Hachinski Ischemic Score of less than or equal to 4[25]; permitted medications stable for 4 weeks prior to screening; a Geriatric Depression Scale score of less than 6[26]; a study partner with 10 or more hours per week of contact either in person or on the telephone and who could accompany the participant to the clinical visits; visual and auditory acuity adequate for neuropsychological testing; good general health with no diseases precluding enrolment; 6 grades of education or work history equivalent; and ability to speak English or Spanish fluently. Women had to be sterile or 2 years past childbearing potential.

At the screening visit, all participants were required to provide informed consent as compatible with the local sites (Institutional Review Board regulations). In addition, all participants provided demographics, family history, and medical history. All participants were given a physical examination and a neurologic examination, and vital signs were recorded. The haplotype of apolipoprotein E (APOE) gene was assessed on blood

samples. Cerebrospinal fluid samples were collected in a subgroup of the participants: Amyloid-β_{1-42}, total Tau, and phosphorylated Tau_{181} measurements were completed using the Roche Elecsys Cobas E601 fully automated immunoassay platform at the ADNI biomarker core (University of Pennsylvania) and were available for 61.3%, 61.2%, and 61.2% of the participants included in our analysis, respectively.

Data on amyloid tracers uptake on Positron Emission Tomography (PET), including florbetapir (AV-45), florbetaben (FBB), and Pittsburgh compound B (PiB), were available in 66.7% of participants. Quantitative measurements of standardised uptake value ratio (SUVR) were provided by the ADNI PET core (University of California, Berkeley) following protocols described in the ADNI website (https://adni.loni.usc.edu/methods/pet-analysis-method/).

Participants were classified as amyloid-positive based on abnormal amyloid level detected on cerebrospinal fluid (<1098 pg/ml)[27] or PET (thresholds recommended in the ADNI PET core documentation: AV-45 > 1.11,[28] FBB > 1.08,[29] PiB > 1.5[30]), and as tau-positive based on abnormal level of total tau (>242 pg/ml) or phosphorylated tau (>19.2) on cerebrospinal fluid.[27]

Perfusion measurements from Arterial Spin Labelling MRI were available in a subsample of 1199 scans acquired on 455 participants, and were performed by the University of California, San Francisco, following protocols described in the ADNI website. The Arterial Spin Labelling techniques included 227 3D pseudo-continuous arterial spin labelling (pCASL) and 972 pulsed arterial spin labelling (PASL, 959 2D and 13 3D).

NACC

The NACC database comprises data collected from the Alzheimer's Disease Centres in the United States funded by the National Institute on Ageing. From 2005 to the present, these centres have been contributing data to the Uniform Data Set using a prospective, standardised, and longitudinal clinical evaluation of the enrolled participants, including both participants without any cognitive impairment and participants with cognitive impairment and dementia. Participants are enrolled on a referral or volunteer basis and undergo a complete examination yielding demographic data, neuropsychological testing scores, and clinical diagnosis. The haplotype of APOE is run independently by each Alzheimer's Disease Centre and reported in the NACC database. Cerebrospinal fluid samples were collected in a subsample of the participants: Amyloid-β_{1-42}, total Tau, and phosphorylated Tau_{181} measurements were available in 363 (including 206 obtained through enzyme-linked immunosorbent assay, ELISA, and 157 through Luminex), 355 (including 193 ELISA and 162 Luminex), and 349 (including 192 ELISA and 157 Luminex) participants, respectively. A clinical report of abnormal level of amyloid and tau in cerebrospinal fluid was also available in 96 and 91 participants, respectively. Amyloid PET scans were available in 206 participants (111 AV-45 and 95 FBB) and were visually assessed for amyloid positivity by an experienced physician-scientist. A clinical report of abnormal uptake of amyloid and tau tracers in PET were also available in 432 and 26 participants, respectively. Participants were classified as amyloid-positive based on abnormal amyloid level detected on cerebrospinal fluid (<570 pg/ml for ELISA[31] or <192 pg/ml for Luminex[32]) or on PET (visually) or as indicated in the clinical report, and as tau-positive based on abnormal level of total tau (>412 pg/ml for ELISA[31] and >93 pg/ml for Luminex[32]) or phosphorylated tau (>78 pg/ml for ELISA[31] and >23 pg/ml for Luminex[32]) on cerebrospinal fluid or as indicated in the clinical report.

Perfusion measurements from Arterial Spin Labelling MRI were available in a subsample of 439 participants, and were performed with an automated pipeline[33] with partial volume correction.[34] The Arterial Spin Labelling techniques included 409 3D pCASL and 30 PASL (22 3D and 8 2D).

OASIS

OASIS-3 is a retrospective compilation of data collected over the course of 15 years as part of research studies at Washington University in St. Louis.[23] All procedures were approved by the Institutional Review Board of Washington University School of Medicine. Participants were recruited from the community via flyers, word of mouth, and community engagements.[23] Enrolled participants were considered generally healthy or without medical conditions that precluded longitudinal participation or contraindications to study procedures, such as MRI and lumbar puncture.[23] Participants underwent clinical assessments which comprised collection of medical and family history, physical examination, and neuropsychological evaluation.[23] No cerebrospinal fluid data were available for the participants included in our analysis. Data on amyloid and tau tracers uptake on PET were available in 73.3% and 31.2% of participants, respectively. Amyloid tracers included AV-45 in 336 cases and PiB in 656 cases, whereas the employed tau tracer was Flortaucipir (18F-AV-1451). Quantitative measurements of the tracer uptake were provided in OASIS-3. The acquisition and processing protocols are fully described in the OASIS-3 documentation (https://www.oasis-brains.org/files/OASIS-3_Imaging_Data_Dictionary_v2.3.pdf). We used the cutoff values recommended in the OASIS-3 documentation to classify participants as amyloid-positive (Centiloid AV-45 > 20.6 or Centiloid PiB > 16.4) and as tau-positive (AV-1451 Tauopathy > 1.22).

Perfusion measurements from Arterial Spin Labelling MRI (2D PASL) were available in a subsample of 595 participants, and were performed with an automated pipeline[33] with partial volume correction.[34]

Ethics

All participants gave written informed consent prior to participation. All studies were approved by study sites' respective regional ethics committees.

The Ethics committees/institutional review boards that approved the ADNI study are: Albany Medical Centre Committee on Research Involving Human Subjects Institutional Review Board, Boston University Medical Campus and Boston Medical Centre Institutional Review Board, Butler Hospital Institutional Review Board, Cleveland Clinic Institutional Review Board, Columbia University Medical Centre Institutional Review Board, Duke University Health System Institutional Review Board, Emory Institutional Review Board, Georgetown University Institutional Review Board, Health Sciences Institutional Review Board, Houston Methodist Institutional Review Board, Howard University Office of Regulatory Research Compliance, Icahn School of Medicine at Mount Sinai Program for the Protection of Human Subjects, Indiana University Institutional Review Board, Institutional Review Board of Baylor College of Medicine, Jewish General Hospital Research Ethics Board, Johns Hopkins Medicine Institutional Review Board, Lifespan—Rhode Island Hospital Institutional Review Board, Mayo Clinic Institutional Review Board, Mount Sinai Medical Centre Institutional Review Board, Nathan Kline Institute for Psychiatric Research & Rockland Psychiatric Centre Institutional Review Board, New York University Langone Medical Centre School of Medicine Institutional Review Board, Northwestern University Institutional Review Board, Oregon Health and Science University Institutional Review Board, Partners Human Research Committee Research Ethics, Board Sunnybrook Health Sciences Centre, Roper St. Francis Healthcare Institutional Review Board, Rush University Medical Centre Institutional Review Board, St. Joseph's Phoenix Institutional Review Board, Stanford Institutional Review Board, The Ohio State University Institutional Review Board, University Hospitals Cleveland Medical Centre Institutional Review Board, University of Alabama Office of the IRB, University of British Columbia Research Ethics Board, University of California Davis Institutional Review Board Administration, University of California Los Angeles Office of the Human Research Protection Program, University of California San Diego Human Research Protections Program, University of California San Francisco Human Research Protection Program, University of Iowa Institutional Review Board, University of Kansas Medical Centre Human Subjects Committee, University of Kentucky Medical Institutional Review Board, University of Michigan Medical School Institutional Review Board, University of Pennsylvania Institutional Review Board, University of Pittsburgh Institutional Review Board, University of Rochester Research Subjects Review Board, University of South Florida Institutional Review Board, University of Southern California Institutional Review Board, University of Texas Southwestern Institution Review Board, VA Long Beach Healthcare System Institutional Review Board, Vanderbilt University Medical Centre Institutional Review Board, Wake Forest School of Medicine Institutional Review Board, Washington University School of Medicine Institutional Review Board, Western Institutional Review Board, Western University Health Sciences Research Ethics Board, and Yale University Institutional Review Board.

The Ethics committees/institutional review boards that approved the data collection for NACC database are: University of Alabama Office of the IRB, Arizona State University Institutional Review Board, Banner Health Institutional Review Board, Barrow Neurological Institute Institutional Review Board, the University of Arizona Human Subjects Protection Program, Stanford Institutional Review Board, University of California Davis Institutional Review Board Administration, University of California Los Angeles Office of the Human Research Protection Program, University of California San Diego Human Research Protections Program, University of California San Francisco Human Research Protection Program, University of California Irvine Office of Research Human Research Protections, University of Southern California Institutional Review Board, Yale University Institutional Review Board, Mayo Clinic Institutional Review Board, University of Florida Institutional Review Boards, Emory Institutional Review Board, Northwestern University Institutional Review Board, Rush University Medical Centre Institutional Review Board, Indiana University Institutional Review Board, University of Kansas Medical Centre Human Subjects Committee, University of Kentucky Medical Institutional Review Board, Johns Hopkins Medicine Institutional Review Board, Boston University Medical Campus and Boston Medical Centre Institutional Review Board, the Human Research Protection Program at Mass General Brigham, Michigan Medical School Institutional Review Board, Washington University School of Medicine Institutional Review Board, Columbia University Medical Centre Institutional Review Board, Icahn School of Medicine at Mount Sinai Program for the Protection of Human Subjects, the University of Nex Mexico Institutional Review Board, New York University Langone Medical Centre School of Medicine Institutional Review Board, Duke University Health System Institutional Review Board, Wake Forest School of Medicine Institutional Review Board, Cleveland Clinic Institutional Review Board, University Hospitals Cleveland Medical Centre Institutional Review Board, Oregon Health and Science University Institutional Review Board, University of Pennsylvania Institutional Review Board, University of Pittsburgh Institutional Review Board, Vanderbilt University Medical Centre Institutional Review Board, University of Texas Health Science Centre at San Antonio Office of the Institutional Review Board,

the University of Washington Office of Research Human Subject Division, the University of Wisconsin–Madison Human Research Protection Program.

For OASIS, all procedures were approved by the Institutional Review Board of Washington University School of Medicine.

Assessment of cognitive status and dementia

In all three cohorts, the Clinical Dementia Rating (CDR) assessment[35] was performed through standardised interview with the participant and a knowledgeable informant. Six categories of cognitive functioning (memory, orientation, judgment and problem solving, community affairs, home and hobbies, and personal care) were assessed. We used the standard CDR global score cutoff value of 1 to classify participants as with dementia (1 and above) or without dementia. The Mini-Mental Status Examination[36] (MMSE) scores were available in a subgroup of 7046 participants and were used only in sensitivity analyses. MMSE evaluates orientation, memory, attention, concentration, naming, repetition, comprehension, and ability to create a sentence and to copy 2 overlapping pentagons.[36] The clinical diagnoses followed the criteria established by the National Institute of Neurological and Communicative Disorders and Stroke (NINCDS) and the Alzheimer's Disease and Related Disorders Association (ADRDA),[37,38] as recommended in the National Alzheimer's Coordinating Centre's Uniform Data Set. For this study, we did not categorise participants based on the clinical diagnosis when available due to the variable availability of biomarkers useful for the diagnosis in each participant, the revision of the NINCDS/ADRDA criteria occurred during the study period, and the variability in the diagnostic process within and across the studies, which could be performed by either a consensus panel or a single physician depending on a given centre practice.

MRI data processing

MRI data were acquired with a variety of 1.5- and 3-T MRI scanners and sequences (Table 1). All T1-weighted images were processed using the *recon-all* module of the freely available FreeSurfer software package (v7.4),[39] which resampled all the images to 1 mm isotropic resolution and performed an atlas-based brain parcellation. The longitudinal processing scheme was used for estimating brain atrophy (grey and white matter volumes, and cortical thickness) longitudinally.[40] White matter lesions were segmented with a previously validated approach on T1-weighted images.[41] We classified as periventricular WML the clusters of WML adjacent to the lateral ventricles; the remaining clusters of WML were classified as deep WML.

Robust PVS segmentation method development and validation

PVS were segmented using a novel approach that advances previous techniques[10–15] being fully-automated and showing excellent inter-scanner reproducibility (Fig. 2). We employed the filter developed by Frangi et al.[16] to enhance tubular, vessel-like structures on T1-weighted images and generate "vesselness maps" as previously described.[17,42] Briefly, the Frangi filter enhances tubular, vessel-like structures on a grey-scale image and assigns a "vesselness" value to each voxel $\mathscr{V}(s)$ from eigenvectors λ of the Hessian matrix $\mathscr{H}$ of the image as:

$$\mathscr{V}(s)=\begin{cases} 0 \text{ if } \lambda_2>0 \text{ or } \lambda_3>0, \\ \left(1-\exp\left(-\frac{\mathscr{R}_A^2}{2\alpha^2}\right)\right)\exp\left(-\frac{\mathscr{R}_B^2}{2\beta^2}\right)\left(1-\exp\left(-\frac{\mathscr{S}^2}{2c^2}\right)\right) \end{cases}$$

Where, $\mathscr{R}_A=\frac{|\lambda_1|}{|\lambda_2|}$, $\mathscr{R}_B=\frac{|\lambda_1|}{\sqrt{|\lambda_2\lambda_3|}}$, $S=\|\mathscr{H}\|$.

We and others previously implemented and validated this filter for the segmentation of MRI-visible vascular and perivascular spaces on T1-weighted images using the default, recommended parameters of $\alpha = 0.5$, $\beta = 0.5$, and c set to half the value of the maximum Hessian norm.[12,13,42] This approach requires the user to identify a threshold on the vessel map generated by the filter to define the vessel-like structures: values above that threshold (i.e., with high "vesselness" values) are considered vascular and perivascular spaces, and values below are excluded. However, since the scale of the "vesselness" values generated by the filter differs from image to image (Fig. 2a) depending on the signal intensity values of the input image,[16] and since the signal intensity values on T1-weighted images are represented in arbitrary units which may vary depending on the MRI machine and its calibration, this approach lacks inter-scanner reproducibility[1,9,16–18] (Fig. 2b) and is potentially biased even in longitudinal studies. To overcome this issue, we developed and validated a novel approach for the segmentation of PVS applicable to virtually any type of T1-weighted image.

The MRI data used for this method development and validation were acquired as part of the Biomarkers Consortium for Vascular Contributions to Cognitive Impairment and Dementia (MarkVCID),[43] ADNI,[21] and the Human Connectome Project (HCP development,[44] young adults,[45] and ageing[46]), and included:

a) the MarkVCID inter-scanner reproducibility dataset: 19 participants who underwent four brain MRI scans within an interval of 3–90 days on four different 3-T MRI scanners (General Electric system 750 W, Philips Achieva dStream, Siemens Prisma, and Siemens TIM Trio) from MarkVCID;
b) the inter-field-strength reproducibility dataset: 299 MRI sessions from 115 ADNI participants who underwent in each session two brain MRI scans on the same day with a 1.5- and a 3-T scanner;

FS (T)	Manuf.	Model	TR (sec)	TE (sec)	TI (sec)	FA (°)	Native voxel vol. (mm^3)	Overall (N = 20,845) N (%)	ADNI (N = 10,977) N (%)	NACC (N = 7819) N (%)	OASIS (N = 2049) N (%)
1.5	GE	GENESIS SIGNA	0.009–0.035	0.002–0.008	0.45–1	8–60	1.2	1641 (7.9)	271 (2.5)	1370 (17.5)	0
1.5	GE	SIGNA	0.018	0.002–0.003	NA	25	1.8	50 (0.2)	0	50 (0.6)	0
1.5	GE	SIGNA EXCITE	0.008–0.029	0.002–0.004	0.5–1	8–25	1.1	999 (4.8)	909 (8.3)	90 (1.2)	0
1.5	GE	SIGNA HDx	0.009–0.011	0.004	0.5–1	8–10	1.1	587 (2.8)	425 (3.9)	162 (2.1)	0
1.5	GE	Signa HDxt	0.009–0.02	0.004–0.007	0.45–1	8–30	1.1	572 (2.7)	303 (2.8)	269 (3.4)	0
1.5	Hitachi	OASIS	NA	NA	NA	NA	0.2	1 (0.0)	0	1 (0.0)	0
1.5	Philips	Achieva	0.009	0.004	1	8	1.1	70 (0.3)	70 (0.6)	0	0
1.5	Philips	Eclipse 1.5T	0.009	0.002	NA	15	1.5	74 (0.4)	0	74 (0.9)	0
1.5	Philips	Gyroscan Intera	0.008–0.009	0.004	0.761–1	8	1.1	13 (0.1)	12 (0.1)	1 (0.0)	0
1.5	Philips	Gyroscan NT	0.009	0.004	1	8	1	19 (0.1)	19 (0.2)	0	0
1.5	Philips	Intera	0.008–0.01	0.003–0.004	1–1.076	8	1.1	359 (1.7)	352 (3.2)	7 (0.1)	0
1.5	Philips	Intera Achieva	0.009	0.004	1	8	1.1	6 (0.0)	6 (0.1)	0	0
1.5	Siemens	Aera	NA	NA	0.8	NA	1	7 (0.0)	0	7 (0.1)	0
1.5	Siemens	Avanto	1.7–2.4	0.002–0.004	1–1.1	8–15	1.9	452 (2.2)	443 (4.0)	7 (0.1)	2 (0.1)
1.5	Siemens	Espree	0.011–2.4	0.003–0.006	1–1.1	8–25	1.8	36 (0.2)	24 (0.2)	12 (0.2)	0
1.5	Siemens	Magnetom VISION	NA	NA	0.3	NA	1.8	2 (0.0)	0	2 (0.0)	0
1.5	Siemens	Magnetom ESSENZA	1.85	0.003	1.1	9	1	1 (0.0)	0	1 (0.0)	0
1.5	Siemens	NUMARIS/4	2.4	0.004	1	8	1.9	2 (0.0)	2 (0.0)	0	0
1.5	Siemens	Sonata	1.9–3	0.003–0.005	0.93–1.1	8–20	1.8	498 (2.4)	376 (3.4)	88 (1.1)	34 (1.7)
1.5	Siemens	Sonata Vision	2.4–3	0.004	1	8	1.9	40 (0.2)	40 (0.4)	0	0
1.5	Siemens	Symphony	2–3	0.003–0.004	1–1.1	8–15	1.9	681 (3.3)	594 (5.4)	87 (1.1)	0
1.5	Siemens	Symphony Tim	2.4–3	0.002–0.004	1	8	1.9	126 (0.6)	124 (1.1)	2 (0.0)	0
1.5	Siemens	Vision	9.7	4	NA	10	1.3	172 (0.8)	0	0	172 (8.4)
3	GE	Discovery MR750	0.006–0.009	0.002–0.003	0.4–1.06	8–12	1.1	2990 (14.3)	958 (8.7)	2032 (26.0)	0
3	GE	Discovery MR750w	0.008	0.003	0.4	11	1.1	132 (0.6)	132 (1.2)	0	0
3	GE	GENESIS SIGNA	0.007	0.003	0.9	8	1.2	18 (0.1)	18 (0.2)	0	0
3	GE	SIGNA EXCITE	0.007–0.008	0.003	0.45–0.9	8–15	1.2	50 (0.2)	44 (0.4)	6 (0.1)	0
3	GE	SIGNA HDx	0.007	0.003	0.4–0.9	8–11	1.3	53 (0.3)	53 (0.5)	0	0
3	GE	Signa HDxt	0.005–0.02	0.002–0.004	0.4–0.9	8–27	1.2	658 (3.2)	427 (3.9)	231 (3.0)	0
3	GE	Signa MR360	2.1	0.003	0.9	8	1	1 (0.0)	0	1 (0.0)	0
3	GE	SIGNA PET/MR	0.008	0.003	0.4	11	1.3	77 (0.4)	0	77 (1.0)	0
3	GE	SIGNA Premier	0.007	0.003	0.4–0.45	11–12	1	89 (0.4)	56 (0.5)	33 (0.4)	0
3	GE	SIGNA UHP	0.007–2.077	0.003	0.4–0.9	8–11	1	10 (0.0)	7 (0.1)	3 (0.0)	0
3	Philips	Achieva	0.006–0.007	0.003	0.805–0.9	8–9	1.2	889 (4.3)	597 (5.4)	292 (3.7)	0
3	Philips	Achieva dStream	0.006–0.007	0.003	NA	8–9	1	186 (0.9)	138 (1.3)	48 (0.6)	0
3	Philips	GEMINI	0.007	0.003	NA	9	1.2	44 (0.2)	35 (0.3)	9 (0.1)	0
3	Philips	Ingenia	0.007	0.003	0.9	9	1.1	209 (1.0)	209 (1.9)	0	0
3	Philips	Ingenia Elition X	0.007	0.003	NA	9	1	14 (0.1)	14 (0.1)	0	0
3	Philips	Ingenuity	0.007	0.003	NA	9	1.3	19 (0.1)	16 (0.1)	3 (0.0)	0
3	Philips	Intera	0.007	0.003	0.845–0.869	8–9	1.2	273 (1.3)	273 (2.5)	0	0
3	Philips	Intera Achieva	0.007	0.003	0.855	8	1.2	1 (0.0)	1 (0.0)	0	0
3	Siemens	Allegra	2.3–2.5	0.003–0.004	0.9–1.1	8–9	1.1	136 (0.7)	108 (1.0)	28 (0.4)	0
3	Siemens	Biograph mMR	2.3–2.4	0.002–0.003	0.9–1	8–9	1.3	584 (2.8)	26 (0.2)	5 (0.1)	553 (27.0)
3	Siemens	Magnetom Prisma Fit	2.3	0.003	0.9	9	1	12 (0.1)	12 (0.1)	0	0
3	Siemens	Magnetom Vida	2.3–2.4	0.003	0.9	8–9	1.2	219 (1.1)	3 (0.0)	1 (0.0)	215 (10.5)
3	Siemens	Prisma	2.3–2.4	0.002–0.003	0.9–1.06	8–9	1	957 (4.6)	255 (2.3)	702 (9.0)	0
3	Siemens	Prisma fit	1.8–2.4	0.002–0.005	0.9–1	8–10	1	810 (3.9)	663 (6.0)	146 (1.9)	1 (0.0)
3	Siemens	Skyra	1.8–2.3	0.002–0.003	0.649–0.962	8–10	1.1	1696 (8.1)	489 (4.5)	1207 (15.4)	0
3	Siemens	Skyra fit	2.3	0.003	0.9	9	1	26 (0.1)	26 (0.2)	0	0
3	Siemens	Trio	1.62–2.5	0.002–0.004	0.9–1.1	7–15	1.2	144 (0.7)	121 (1.1)	23 (0.3)	0

(Table 1 continues on next page)

FS (T)	Manuf.	Model	TR (sec)	TE (sec)	TI (sec)	FA (°)	Native voxel vol. (mm^3)	Overall (N = 20,845) N (%)	ADNI (N = 10,977) N (%)	NACC (N = 7819) N (%)	OASIS (N = 2049) N (%)
(Continued from previous page)											
3	Siemens	TrioTim	1.31–3.2	0.002–0.455	0.9–1.2	7–120	1.1	3098 (14.9)	1547 (14.1)	479 (6.1)	1072 (52.3)
3	Siemens	Verio	1.7–2.3	0.002–0.004	0.9	8–9	1.2	805 (3.9)	767 (7.0)	38 (0.5)	0
Not available/unknown			0.007–2.3	0.002–0.005	0.4–0.9	8–60	1	237 (1.1)	12 (0.1)	225 (2.9)	0

FA: Flip Angle (degree, °); FS: Field Strength (Tesla, T); TE: Time to Echo (seconds); TI: Inversion Time (seconds); TR: Repetition Time (seconds). Native voxel volume is the volume of a single voxel in the original image.

Table 1: **Overview of the MRI scanners and parameters employed to acquire the T1-weighted images analysed in the study.**

c) the MarkVCID test-retest dataset: 39 participants from MarkVCID who underwent two brain MRI scans on the same MRI scanner using the same protocol within an interval of 1–14 days;
d) the biological validation dataset: 2163 healthy participants from the HCP whose MRI-visible vascular and perivascular spaces have been studied extensively,[47–49] providing a reference for verifying established associations.

Supplementary Tables S17 and S18 include the details for the baseline characteristics of the analysed participants and the MRI protocols employed in each of the above datasets, respectively.

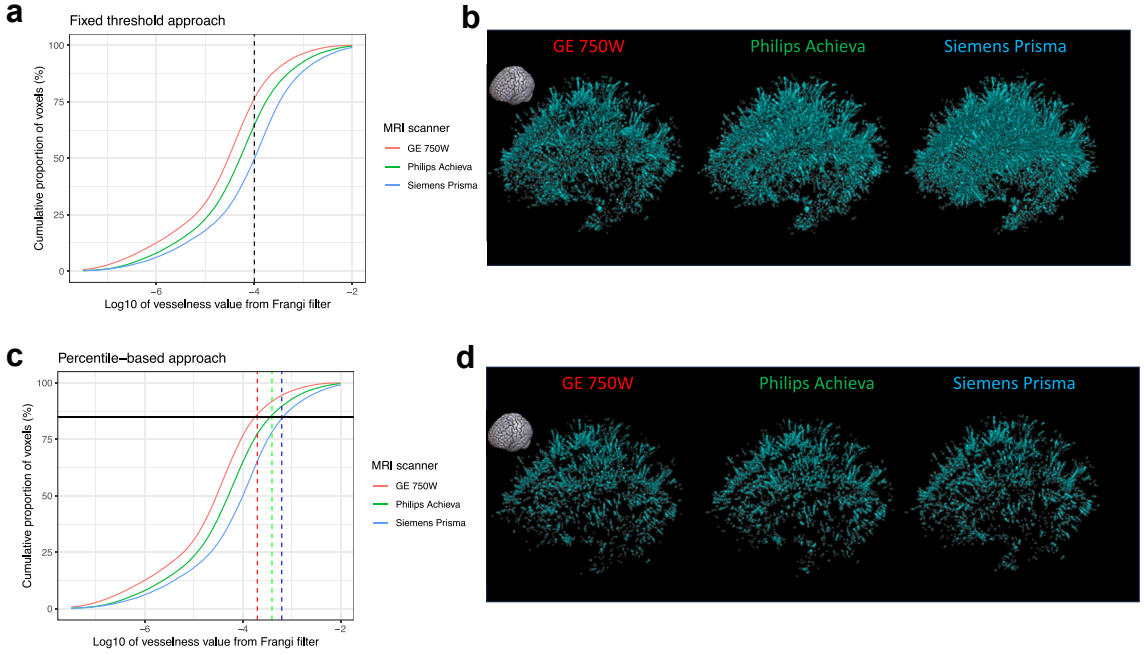

Fig. 2: **Comparison between the original approach and our novel approach.** The original approach requires to set a single threshold (black vertical dashed line in panel a, in this case equal to 10^{-4}), and to use this threshold to segment vessel-like structures (Panel a). However, this approach lacks inter-scanner reproducibility, because the scale of the vesselness maps depends on the signal intensity of the input image, which may differ among MRI scanners and protocols. In fact, in this example the threshold would lead to very different number of segmented voxels: vessel-like masks from Siemens scanner will have approximately 12.5 and 25% more voxels than those from Philips and GE scanners, respectively (Panel b). In our novel approach, we set specific thresholds to the individual images (vertical dashed lines, red for the GE-derived image, green for the Philips-derived image, and blue for the Siemens-derived image) based on the value of the voxel corresponding to the 85th percentile (black horizontal solid line) of the total number of non-zero voxels of the vesselness map (Panel c). This approach leads to consistent PVS masks (Panel d) and robust metrics derived from the PVS masks (Supplementary Figs. S3a–c and S5), while preserving inter-individual differences and accuracy (Supplementary Figs. S3d–f and S4). Panels b and d report the 3D representations of the PVS segmentation masks of the same participant obtained with 3 different MRI scanners with fixed threshold approach (panel b) and our novel percentile-based approach (panel d). The small brain icon on the top left of each panel indicates the orientation of the PVS masks.

Our novel approach is based on the observation that the total number of voxels with non-zero vesselness value obtained from the Frangi filter applied on T1-weighted images is:

1) Consistent across brain images of the same participant acquired with different MRI scanners (inter-scanner and inter-field-strength reproducibility, Supplementary Fig. S1a and b, respectively);
2) Consistent across brain images of the same participant acquired on two different MRI sessions with the same MRI scanner and protocol (test-retest repeatability, Supplementary Fig. S1c);
3) Significantly associated with age, sex, and body mass index (Supplementary Fig. S1d–f) as previously described for PVS.[47–49]

Therefore, we hypothesised that the value of the voxel corresponding to a single, specific percentile of the total number of voxels with non-zero "vesselness" values could be used as a threshold for consistently and robustly segmenting MRI-visible vessel-like structures across different types of T1-weighted images (Fig. 2c and d). We identified this percentile to be 85% in the white matter, based on the average ratio between the number of voxels that we previously segmented as vascular and perivascular spaces in the HCP dataset[47,48] and the corresponding total number of voxels with non-zero vesselness value.

In each individual vesselness map generated by the Frangi filter, the vesselness value corresponding to the 85th percentile of the total number of non-zero voxels was automatically computed: the voxels with vesselness value above this threshold were retained and binarised to make the PVS mask, whereas those below or equal to the threshold were excluded. To improve the specificity of the PVS segmentation,[17,42] the Frangi filter was applied on FreeSurfer's white matter mask with the following modifications: the voxels labelled as corpus callosum by FreeSurfer were excluded; periventricular areas were excluded by subtracting FreeSurfer's lateral ventricle binary mask enlarged by 3 units from the white matter binary mask; WML were also excluded. Finally, we used MATLAB's *regionprops3* function with the default 26-connected neighborhood definition to compute PVS count and mean diameter across all PVS clusters with in-plane size of at least 2 voxels detected in the modified white matter mask of each image.

Accuracy of the PVS segmentation was assessed via visual inspection and quantified with the Dice similarity coefficient using as a reference the PVS masks obtained with an established and previously validated technique applied on the HCP dataset.[12,13,17,49] The Dice similarity coefficient ranges from 0, indicating no spatial overlap between two sets of binary segmentation masks, to 1, indicating complete overlap.

The robustness of the PVS metrics assessed in our study (i.e., PVS count and PVS mean diameter) across different MRI scanners (inter-scanner and inter-field-strength reproducibility) and sessions (test-retest repeatability) was assessed with the intraclass correlation coefficients, ranging from 0 to 1, where a higher value indicates higher agreement between the compared modalities. Similar evaluations were also performed for WML metrics.

Since typically FLAIR and T2-weighted images are considered more sensitive to WML and PVS, respectively,[8,9] due to a higher contrast between the cerebral parenchyma and the WML/PVS, we also evaluated the suitability of assessing WML and PVS with only the T1-weighted images in two ways: 1) we measured the correlation between the number of WML/PVS voxels measured on T1-weighted versus FLAIR/T2-weighted images, to determine the strength and direction of their relationship; 2) to confirm the spatial agreement of the WML/PVS voxels across the two modalities, we measured the overlap of the WML/PVS voxels identified on T1-weighted images with the WML/PVS voxels (and the adjacent 3 voxels to account for any residual misalignment between the imaging modalities) identified from FLAIR/T2-weighted images rigidly registered to the corresponding T1-weighted images.

Statistics

All the models and simulations described below were adjusted for intracranial volume and the following baseline factors (as reported on the documented clinical assessment and participant health history): age, sex, educational level, race, body mass index, CDR global score, family history of dementia (positive if any of the participants' parents were reported to have dementia), and history of hypertension, dyslipidaemia, diabetes, and cardio-/cerebro-vascular disease (i.e., any of the following: heart failure, angina, cardiac arrest, stent placement, coronary artery bypass, pacemaker, defibrillator, heart valve replacement or repair, stroke, transient ischemic attack). Potential confounders were selected based on the modified disjunctive cause criterion,[50] identifying demographic and clinical variables that have an association with the exposure and/or the outcome, as supported by findings from the scientific literature. Data for these factors were all available for more than 97% participants. The proportion of participants with at least one variable with missing value was 7.4% of the total sample size (5.4% in ADNI, 8.7% in NACC, and 9.8% in OASIS). We used missing indicators for handling missing values in the covariates. For the main analyses, we also employed multivariate imputation by chained equations with 5 imputations and predictive mean matching[51] and verified the consistency of the results.

The associations of our PVS markers with cognitive status (non-dementia versus dementia) and the other

covariates at the baseline visit were assessed with general linear models stratified according to study. The association of our PVS markers at the baseline with subsequent risk of developing dementia was assessed in each study independently with Cox proportional-hazards models and the results were integrated using a random-effects meta-analysis with the Hartung-Knapp-Sidik-Jonkman method[52] to account for potential differences among the studies (two-stage pooled analysis). Inter-study heterogeneity was assessed statistically with the I^2. Person-time was calculated in each participant from the baseline clinical visit (origin and start times) until the visit where the dementia was documented or the last clinical visit, whichever occurred first (end time). The proportional-hazards assumptions were verified by assessing the relationship between Schoenfeld residuals and time.[53] Additionally, we analysed these associations by combining in the same model all the participant-level data (simple pooled analysis), stratified according to study and adjusted for the same covariates, and used penalised splines to assess their deviation from linearity.[54] We used the P-spline method[55] as implemented by Therenau and Grambsch.[56] The basis functions were 3rd degree polynomials (cubic splines). We chose 4 degrees of freedom and the number of basis functions (knots) was set equal to 10.[56–58] This way the spline model can include enough basis functions to capture relevant data patterns without being excessively complex. Knots included 2 boundary knots corresponding to the minimal and maximal value of the vascular marker, and 8 equidistant interior knots (12.5th, 25th, 37.5th, 50th, 62.5th, 75th, and 87.5th percentiles). A penalty term was applied to prevent overfitting, and the amount of penalization was controlled by a tuning parameter (smoothness level λ). Here we used the second differences of the spline coefficients as penalty term, and λ was calculated iteratively until a fit with the requested degrees of freedom was achieved.[55,56] Linearity of the association was then assessed with the chi-square testing for zero slope in a regression of the spline coefficients on the centres of the basis functions.[56] In addition to the covariates used in all the other models, the linear models and Cox-regression models above were also controlled for the time interval between the MRI scan and the clinical visit of the cognitive assessment at the baseline.

Linear mixed-effects models with random intercepts and slopes for each participant were used to estimate the longitudinal trajectories of grey matter volume, cortical thickness, and white matter volume according to baseline PVS count or mean diameter. In addition to the covariates used in all the other models, the linear mixed-effects models were also adjusted for the value of the dependent variable at baseline, and the following characteristics of the MRI scanner that may influence the longitudinal estimation of brain atrophy: field strength, manufacturer, and intra-individual consistency of the protocol used for the longitudinal MRI acquisitions (consistent versus non-consistent protocol). Interaction terms between time and all predictors were included as well to estimate the marginal per-year effects of each predictor. Linear mixed-effects models with random intercepts and slopes for each participant were also used to estimate and compare the longitudinal trajectories of PVS and WML markers in participants without dementia who converted to dementia versus non-converters. In all linear mixed-effects models, the random effects were assumed to follow a bivariate normal distribution.

For all the general linear models and linear mixed-effects models, normality of residuals was assessed with quantile–quantile plots, homoscedasticity of residuals was assessed visually by plotting residuals and fitted values, and linearity of quantitative predictors was assessed visually by plotting residuals and quantitative predictors.

Sensitivity analyses for all the models above included: 1) the individual assessment of other potential confounding factors available only in a subsample of the participants (92.6% history of tobacco smoking, 90.0% Apolipoprotein E alleles, 39.0% amyloid-β and 24.7% tau status as assessed on cerebrospinal fluid and/or Positron-Emission Tomography); 2) the use of MMSE rather than CDR for the cognitive evaluation (available in 70.3% of the participants); 3) the assessment of MRI acquisition artifacts or factors that could have influenced the estimation of the vascular markers. In sensitivity analyses, hazard ratios were estimated from Cox models with stratification according to study cohort (simple pooled analysis) owing to smaller sample sizes in the individual studies.

To evaluate the potential utility of PVS markers as a screening tool in clinical trials, we computed the sample size needed to detect improvements in cognitive decline trajectories when restricting the sample based on the baseline values of the marker, and compared it to the sample size requested without any restriction. The clinical trials were simulated with 1:1 allocation of active treatment and placebo, assuming a 30% treatment effect on cognition over time, and three different trial durations: 48 months, 24 months, or 12 months, with cognitive testing every 12 months, 6 months, or 3 months, respectively. 500 simulations were generated with non-parametric bootstrap iteration and results were summarised with mean and standard error. Additionally, we used binomial logistic regression (controlling for the same covariates used in all the other models) to estimate the probability that participants in the higher risk tertiles for our markers were also positive for amyloid-β or tau. The linearity assumption for quantitative predictors was assessed with the Box–Tidwell test.[59]

The robustness of the PVS and WML metrics analysed in our study across different MRI scanners (inter-scanner and inter-field-strength reproducibility) and

sessions (test-retest repeatability) was assessed with the intraclass correlation coefficients [ICC(2,k), two-way random, average score], ranging from 0 to 1, where a higher value indicates higher agreement between the compared modalities. Correlations were assessed with the Spearman rank-order correlation coefficient. Differences between groups were assessed with the Wilcoxon rank-sum test.

All the analyses were based on *a priori* hypotheses, but to account for two variables of interest (PVS count and mean diameter), we present P values that were corrected for multiple comparisons with the use of the Holm–Bonferroni procedure.[60] In brain regional analyses, the correction for multiple comparisons was performed across all the analysed regions. All statistical analyses were performed in R v4.3.3. The following R packages were used for the statistical analyses and generation of the plots: *survival* was used for fitting the Cox proportional-hazards models;[56] *meta* was used for the meta-analysis;[61] *lmer4* was used for fitting the non-linear mixed models;[62] *ggeffects* was used for estimating the marginal effects in the non-linear mixed models;[63] *longpower* was used for the simulation of clinical trials;[64] *ggseg* was used for generating the plots with the brain statistics;[65] *ggplot2* was used for generating all the other plots.[66]

Role of funders

The funders had no role in the design of this analysis, data analysis, interpretation of data, or writing of the report.

Results

Technical validation of PVS markers

The spatial overlap between the PVS masks obtained with our fully-automated approach and those obtained with a previously validated semi-automated technique[12,13,17] was very high (Dice similarity coefficient: 0.95 ± 0.0001) and the numbers of PVS voxels identified with the two methods were strongly correlated (Supplementary Fig. S2a). Consistently, PVS measured with our method also showed a strong positive association with age, male sex, and body mass index in the Human Connectome Project dataset (Supplementary Fig. S2b–d), replicating results previously published with the validated semi-automated techniques.[47–49] These data support the reliability and accuracy of our PVS masks. While previous methods are user-dependent (i.e., the user needs to identify a threshold for each type of T1-weighted image) and lack inter-scanner reproducibility of PVS markers[1,9,16–18] (Fig. 2a and b), our technique is able to provide measurements of PVS count and diameter in a fully automated and robust way (Fig. 2c and d). Indeed, both metrics showed excellent intraclass correlation coefficients (≥0.9 for WM-PVS and ≥0.8 for BG-PVS) for inter-scanner reproducibility, inter-field-strength reproducibility, and test-retest repeatability (Supplementary Fig. S3). We also observed a strong correlation between the numbers of PVS voxels independently identified by our algorithm on the T1- and T2-weighted images (Supplementary Fig. S4a), with an average of 87.3 ± 5.7% of PVS voxels detected on T1-weighted images that overlapped with PVS voxels on T2-weighted images. Overall, these data show that our method can accurately segment PVS on T1-weighted images and that T1-weighted images are suitable to reliably assess PVS morphological metrics and inter-participant differences. In contrast with previous methods,[10–15] our new approach for PVS segmentation is fully automated, requires only T1-weighted images, and provides robust metrics across different scanners and protocols (Supplementary Fig. S3).

Excellent results were also obtained for WML. WML voxels segmented on T1-weighted images were strongly correlated with WML voxels segmented on FLAIR (Supplementary Fig. S4b), with an average of 83.0 ± 0.4% of WML voxels detected on T1-weighted images that overlapped with WML voxels on FLAIR. Moreover, WML volume showed excellent intraclass correlation coefficients (>0.9 for P-WML and >0.8 for D-WML) for inter-scanner reproducibility, inter-field-strength reproducibility, and test-retest repeatability (Supplementary Fig. S5).

Study population

The baseline characteristics of the 10,004 participants stratified by study cohort are reported in Table 2. There were 8867 participants without dementia and 1137 patients with dementia, including 996 clinically diagnosed with probable or possible Alzheimer's dementia, 51 Lewy body dementia, 38 frontotemporal dementia, 1 vascular dementia, and 51 other or uncertain type of dementia. Accuracy of the PVS masks were visually verified for all the cases in a blinded fashion by an expert physician-scientist according to established criteria.[8] We also developed an interactive website that allows the readers to visualise our PVS segmentations and independently verify their accuracy: https://gbarisano.shinyapps.io/pvs-dementia.

In multivariable analyses, all PVS and WML markers were significantly associated with age, sex, body mass index, cognitive scores, and history of hypertension (Supplementary Table S1). History of diabetes was associated with all PVS markers except BG-PVS diameter; history of cardiovascular disease was associated with BG-PVS diameter. In the subgroup analysis (Supplementary Table S2), WM-PVS count was not significantly associated with APOE genotype, amyloid-β or tau status, and BG-PVS count was negatively associated with amyloid-β status and APOE-ε4ε4-carrier status. WM-PVS diameter, P-WML and D-WML volume were associated with positive amyloid-β and APOE-ε4ε4-carrier status. BG-PVS diameter was associated with positive tau and APOE-ε4ε4-carrier status.

Characteristic	Overall (N = 10,004)	ADNI (N = 2621)	NACC (N = 6029)	OASIS (N = 1354)
Age at baseline—yr	71.1 ± 9.7	72.9 ± 7.5	70.6 ± 10.5	70.2 ± 9.2
Sex—N (%)				
Female	5667 (56.6)	1353 (51.6)	3657 (60.7)	742 (54.8)
Male	4337 (43.4)	1268 (48.4)	2372 (39.3)	612 (45.2)
Education – yr	15.7 ± 3.1	16.1 ± 2.7	15.5 ± 3.2	15.8 ± 2.7
Race – %				
White	8474 (84.7)	2302 (87.8)	5041 (83.6)	1131 (83.5)
Black	1163 (11.6)	203 (7.7)	755 (12.5)	205 (15.1)
American Indians	76 (0.8)	6 (0.2)	70 (1.2)	0 (0)
Asian	176 (1.8)	61 (2.3)	107 (1.8)	8 (0.6)
More than one reported	37 (0.4)	34 (1.3)	0	3 (0.2)
Body Mass Index – kg/m^2	27.2 ± 5.2	27.1 ± 5.1	27.1 ± 5.2	27.8 ± 5.4
Dyslipidaemia – N (%)	5274 (52.7)	1387 (52.9)	3242 (53.8)	645 (47.6)
Hypertension – N (%)	4748 (47.5)	1247 (47.6)	2863 (47.5)	638 (47.1)
Diabetes – N (%)	1226 (12.3)	271 (10.3)	811 (13.5)	144 (10.6)
History of cardio-/cerebro-vascular disease – N (%)	2802 (28)	895 (34.1)	1567 (26)	340 (25.1)
Family history of dementia – N (%)	5122 (51.2)	1375 (52.5)	3001 (49.8)	746 (55.1)
History of tobacco smoking[a] – N (%)	3496 (34.9)	637 (24.3)	2273 (37.7)	586 (43.3)
APOE[a] – N (%)				
ε2ε2	29 (0.3)	6 (0.2)	15 (0.2)	8 (0.6)
ε2ε3	807 (8.1)	176 (6.7)	488 (8.1)	143 (10.6)
ε2ε4	213 (2.1)	49 (1.9)	120 (2.0)	44 (3.2)
ε3ε3	4283 (42.8)	1111 (42.4)	2536 (42.1)	636 (47.0)
ε3ε4	2777 (27.8)	809 (30.9)	1532 (25.4)	436 (32.2)
ε4ε4	627 (6.3)	224 (8.5)	325 (5.4)	78 (5.8)
A-beta positivity[a] – N (%)	1957 (50.1)	1277 (62.7)	356 (40.6)	324 (32.7)
Tau positivity[a] – N (%)	1461 (59.2)	1039 (64.7)	232 (53.1)	190 (45.0)
WM-PVS count	441.23 ± 143.63	399.98 ± 130.19	459.77 ± 147.22	438.49 ± 135.31
BG-PVS count	139.69 ± 45.30	122.53 ± 49.72	147.98 ± 43.02	136.02 ± 35.38
WM-PVS mean diameter – mm	1.98 ± 0.14	2.05 ± 0.16	1.95 ± 0.12	1.97 ± 0.12
BG-PVS mean diameter – mm	1.58 ± 0.09	1.63 ± 0.11	1.56 ± 0.08	1.58 ± 0.07
P-WML volume – mm^3	330 (0–1613)	597 (46–1990)	230 (0–1406)	257 (0–1675)
D-WML volume – mm^3	16 (1–72)	34 (7–104)	8 (0–53)	24 (4–90)

Plus–minus values are means ± standard deviations for variables with normal distribution, entries with parentheses are medians (interquartile range) for variables with non-normal distribution. Data on education were missing for 16 (0.16%) participants, on race for 78 (0.8%), on body mass index for 265 (2.6%), on dyslipidaemia for 124 (1.2%), on hypertension for 68 (0.7%), on diabetes for 69 (0.7%), on history of cardio-/cerebro-vascular disease for 46 (0.5%), on family history for dementia for 275 (2.7%). Data from three studies — the Alzheimer's Disease Neuroimaging Initiative (ADNI), the National Alzheimer's Coordinating Centre (NACC), and the Open Access Series of Imaging Studies (OASIS) — are shown. Race was reported by the participant. [a]Total number of subjects with available history of tobacco smoking, Apolipoprotein E (APOE) genotype, amyloid-beta status and tau status were 9267, 8599, 3906, and 2466, respectively.

Table 2: **Baseline characteristics of the study population.**

After controlling for study cohort, demographic, and clinical variables, patients with dementia showed significantly lower WM- and BG-PVS count, higher WM- and BG-PVS diameter, and higher P-WML volume compared with participants without dementia (Supplementary Table S3). Consistent results for PVS count and P-WML were obtained in sensitivity analyses (Supplementary Table S4), indicating that their differences are independent of APOE, amyloid-β, or tau status.

PVS markers and risk of dementia

Among 7518 participants without dementia with at least 1 follow-up visit (Supplementary Table S5), 1493 participants developed dementia during a median follow-up of 4.1 years (interquartile range, 2.3–7.1), including 1306 clinically diagnosed with probable or possible Alzheimer's dementia, 43 Lewy body dementia, 29 frontotemporal dementia, 16 vascular dementia, and 99 other or uncertain type of dementia. In 6025 cases, conversion to dementia did not occur at the last available clinical visit performed in the study (censoring proportion: 80.1%). In the fully adjusted models of the two-stage pooled analysis, each additional 100 WM-PVS and 10 BG-PVS were significantly associated with 20% [95% CI: 13, 26; P = 0.0079, random-effects meta-analysis of Cox proportional-hazards models] and 8% [95% CI: 4, 11; P = 0.011, random-effects meta-analysis of Cox

proportional-hazards models] decreased dementia risk, respectively, and each additional 0.1-mm increase in WM-PVS and BG-PVS mean diameter were significantly associated with 8% [95% CI: 3, 14; P = 0.018, random-effects meta-analysis of Cox proportional-hazards models] and 15% [95% CI: 10, 20; P = 0.0051, random-effects meta-analysis of Cox proportional-hazards models] increased dementia risk, respectively (Fig. 3a–d). P-WML, but not D-WML, was also significantly associated with 13% [95% CI: 6, 20; P = 0.013, random-effects meta-analysis of Cox proportional-hazards models] increased dementia risk (Fig. 3e and f). The spline analysis with pooled data supported a significant linear association over the range of the PVS and P-WML markers measured in this population (Fig. 3g–k) and identified critical threshold values of PVS markers indicating increased risk or protection for dementia: having more than 435 WM-PVS and 135 BG-PVS is significantly associated with lower risk of dementia, whereas WM-PVS and BG-PVS counts below those values are associated with increased dementia risk (Fig. 3g and h); WM- and BG-PVS mean diameters below 1.97 and 1.6 mm, respectively, are significantly associated with lower risk of dementia, while diameters above those values are significantly associated with increased dementia risk (Fig. 3i and j). Similar results were obtained when employing multiple imputation for missing data (Supplementary Fig. S6). Sensitivity analyses showed substantially unchanged results, suggesting that these effects are independent of other potential confounding factors, including the positivity status for amyloid-β or tau biomarkers (Supplementary Fig. S7 and Table S6). The association of WM-PVS diameter with dementia risk lost statistical significance after adding amyloid-β status in the model.

Based on previous results from preclinical studies,[67,68] we hypothesised that one potential mechanism linking PVS with increased risk of dementia could be alterations in cerebral blood flow. Indeed, in most of the brain regions we observed a significant correlation of the regional PVS count and diameter with the corresponding regional cerebral blood flow as assessed *in vivo* with arterial spin labelling MRI (Supplementary Fig. S8). However, after including the mean cortical perfusion as additional covariate in our model, the results remained unchanged for WM-PVS and BG-PVS count and WM-PVS diameter (Supplementary Fig. S7 and Table S6), suggesting that their effect on the risk of dementia is independent of cerebral perfusion.

PVS markers and brain atrophy

Among 3389 participants without dementia with at least 2 MRI scans (Table S7), we investigated the association of PVS and WML markers measured at the baseline MRI with the trajectory of brain atrophy estimated over a total of 14,229 MRI scans (average of 4 scans available per participant) during a median follow-up time of 3.1 years (interquartile range 2.0–5.6 years). In the multivariable mixed-effect models, PVS and WML markers were significantly associated with the longitudinal trajectory of grey matter and cortical thickness atrophy (Fig. 4a and b top rows). Specifically, accelerated atrophy was observed in participants with lower WM-PVS and BG-PVS count and in those with higher WM-PVS and BG-PVS diameter. Each additional 100 WM-PVS and 10 BG-PVS at the baseline was associated with additional 709 [95% CI: 513, 905; P < 0.0001, linear mixed-effects model] and 187 [95% CI: 122, 252; P < 0.0001, linear mixed-effects model] mm^3 of total grey matter preserved per year, respectively; whereas, each additional 0.1 mm increase in WM-PVS and BG-PVS diameter were associated with additional 382 [95% CI: 217, 546; P < 0.0001, linear mixed-effects model] and 576 [95% CI: 308, 844, P < 0.0001, linear mixed-effects model] mm^3 of total grey matter preserved per year. Participants with higher P-WML and D-WML volume at baseline also presented accelerated brain atrophy (Supplementary Table S8). Most of these effects were observed in the temporal lobes, bilaterally, for all PVS markers (Fig. 4a and b bottom rows; Supplementary Tables S9–S11). For white matter volume, only WM-PVS count, BG-PVS count and BG-PVS diameter were significantly associated with accelerated atrophy (Fig. 4c, Supplementary Table S8). Consistent results were obtained when employing multiple imputation for missing data (Supplementary Fig. S9 and Table S8). These effects and their spatial patterns remained significant for most markers in all sensitivity analyses, indicating that the link between these markers and accelerated atrophy is independent of other potential confounding factors, including the positivity status for amyloid-β or tau biomarkers (Supplementary Figs. S10–S12 and Table S12). Exceptions included WM-PVS and BG-PVS diameter, which became not significant after adding tau status in the model for grey matter volume (Supplementary Fig. S10 and Table S12), but remained significant for cortical thickness (Supplementary Fig. S11 and Table S12); BG-PVS diameter became not significant after adding amyloid-β status in the model for white matter volume (Supplementary Fig. S12 and Table S12). Overall, these data showed that fewer WM-PVS and BG-PVS were associated with accelerated brain atrophy. This effect was stronger on the grey matter volume and cortical thickness of the temporal lobes, irrespective of amyloid-β and tau positivity status. Similar associations were found for WM-PVS and BG-PVS diameter, although they were generally less robust when considering amyloid-β and/or tau status in the model.

We further assessed the relationship between the WM-PVS marker measured in a specific lobe and the corresponding atrophy in that lobe. The spatial patterns for regional WM-PVS count (Supplementary Fig. S13a–c) were consistent with those observed in the main model with global WM-PVS count (Fig. 4). Less consistency was

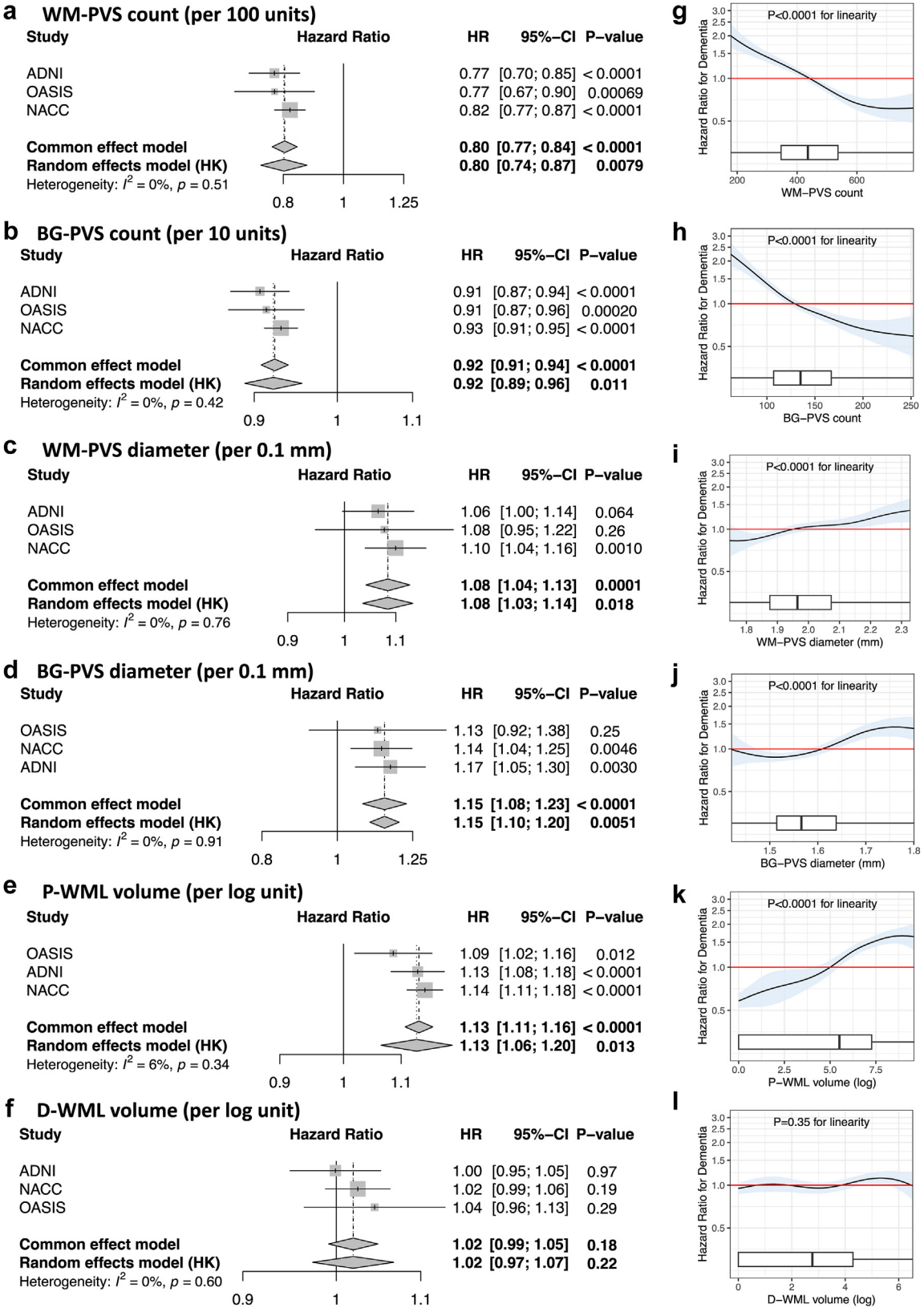
a WM-PVS count (per 100 units)
Study
Hazard Ratio
HR 95%–CI P–value
ADNI 0.77 [0.70; 0.85] < 0.0001
OASIS 0.77 [0.67; 0.90] 0.00069
NACC 0.82 [0.77; 0.87] < 0.0001
Common effect model 0.80 [0.77; 0.84] < 0.0001
Random effects model (HK) 0.80 [0.74; 0.87] 0.0079
Heterogeneity: I^2 = 0%, p = 0.51
0.8 1 1.25
b BG-PVS count (per 10 units)
Study
Hazard Ratio
HR 95%–CI P–value
ADNI 0.91 [0.87; 0.94] < 0.0001
OASIS 0.91 [0.87; 0.96] 0.00020
NACC 0.93 [0.91; 0.95] < 0.0001
Common effect model 0.92 [0.91; 0.94] < 0.0001
Random effects model (HK) 0.92 [0.89; 0.96] 0.011
Heterogeneity: I^2 = 0%, p = 0.42
0.9 1 1.1
c WM-PVS diameter (per 0.1 mm)
Study
Hazard Ratio
HR 95%–CI P–value
ADNI 1.06 [1.00; 1.14] 0.064
OASIS 1.08 [0.95; 1.22] 0.26
NACC 1.10 [1.04; 1.16] 0.0010
Common effect model 1.08 [1.04; 1.13] 0.0001
Random effects model (HK) 1.08 [1.03; 1.14] 0.018
Heterogeneity: I^2 = 0%, p = 0.76
0.9 1 1.1
d BG-PVS diameter (per 0.1 mm)
Study
Hazard Ratio
HR 95%–CI P–value
OASIS 1.13 [0.92; 1.38] 0.25
NACC 1.14 [1.04; 1.25] 0.0046
ADNI 1.17 [1.05; 1.30] 0.0030
Common effect model 1.15 [1.08; 1.23] < 0.0001
Random effects model (HK) 1.15 [1.10; 1.20] 0.0051
Heterogeneity: I^2 = 0%, p = 0.91
0.8 1 1.25
e P-WML volume (per log unit)
Study
Hazard Ratio
HR 95%–CI P–value
OASIS 1.09 [1.02; 1.16] 0.012
ADNI 1.13 [1.08; 1.18] < 0.0001
NACC 1.14 [1.11; 1.18] < 0.0001
Common effect model 1.13 [1.11; 1.16] < 0.0001
Random effects model (HK) 1.13 [1.06; 1.20] 0.013
Heterogeneity: I^2 = 6%, p = 0.34
0.9 1 1.1
f D-WML volume (per log unit)
Study
Hazard Ratio
HR 95%–CI P–value
ADNI 1.00 [0.95; 1.05] 0.97
NACC 1.02 [0.99; 1.06] 0.19
OASIS 1.04 [0.96; 1.13] 0.29
Common effect model 1.02 [0.99; 1.05] 0.18
Random effects model (HK) 1.02 [0.97; 1.07] 0.22
Heterogeneity: I^2 = 0%, p = 0.60
0.9 1 1.1
g
P<0.0001 for linearity
Hazard Ratio for Dementia
WM–PVS count
h
P<0.0001 for linearity
Hazard Ratio for Dementia
BG–PVS count
i
P<0.0001 for linearity
Hazard Ratio for Dementia
WM–PVS diameter (mm)
j
P<0.0001 for linearity
Hazard Ratio for Dementia
BG–PVS diameter (mm)
k
P<0.0001 for linearity
Hazard Ratio for Dementia
P–WML volume (log)
l
P=0.35 for linearity
Hazard Ratio for Dementia
D–WML volume (log)

observed for regional WM-PVS diameter (Supplementary Fig. S13d–f). This suggests a spatial relationship between the atrophy trajectory of a specific brain region and the corresponding WM-PVS count in that region at baseline.

The relatively low sample size of participants with cerebral blood flow data available at the baseline (N = 318) prevented us from building reliable linear mixed-effects models evaluating the relative contribution of cerebral blood flow and PVS to the brain atrophy trajectory while accounting for the relevant clinical and demographic covariates included in all our models.

Longitudinal evolution of PVS markers

We estimated the longitudinal trajectory of the PVS and WML markers in participants without dementia who converted to dementia and compared it with those who did not convert. The WM and BG regions where PVS were measured were spatially-registered and kept consistent across the intra-individual timepoints. All WML voxels at any timepoint were excluded from the PVS analysis in all timepoints. This means that, for each participant, PVS were analysed in the exact same WM and BG voxels across timepoints and none of these voxels included WML in any timepoint. The baseline values and longitudinal trajectories of PVS count and mean diameter significantly differed between converters and non-converters, both in WM and in BG: PVS count at the baseline MRI was significantly lower in converters compared with non-converters (Supplementary Table S13), and further decreased by 3 unit [95% CI: 2, 4; P < 0.0001, linear mixed-effects model] per year. PVS count remained stable in non-converters (Fig. 5a–c). On the other hand, baseline WM-PVS and BG-PVS mean diameter were significantly larger in converters compared with non-converters (Supplementary Table S13), and remained steadily larger over time (Fig. 5b–d). WM-PVS and BG-PVS diameter decreased in non-converters by 2 [95% CI: 1, 4; P = 0.018, linear mixed-effects model] and 3 [95% CI: 2, 5; P < 0.0001, linear mixed-effects model] μm per year. Similar results were obtained when employing multiple imputation for missing data (Supplementary Fig. S14 and Table S14) and in sensitivity analyses (Supplementary Fig. S15 and Table S14), indicating that the different trajectories for these markers in converters versus non-converters were independent of other potential confounding factors such as amyloid-β and tau status. In WM-PVS markers, the differences between converters and non-converters involved mostly the left hemisphere, especially the frontal and parietal lobes (Fig. 5a and b). Significant increases over time in P-WML volume were also found, which were more prominent in converters compared with non-converters (Fig. 5e, Supplementary Table S14). No significant sex-related differences in the trajectories of PVS/WML markers were observed. Overall, these data suggest that changes in PVS count and diameter precede the occurrence of dementia and follow different longitudinal trajectories in dementia converters versus non-converters: in converters, larger baseline PVS remain enlarged, and lower baseline PVS count continue decreasing.

PVS markers in simulated clinical trials

In 48-month placebo-controlled trials simulated with 40,703 cognitive assessments in 7518 participants without dementia, the sample size required to detect a 30% slowing in cognitive decline (assessed with the CDR) with 80% power was lower when selectively screening out participants based on the PVS or the WML markers' tertiles (Supplementary Table S16): sample size reductions were 13–37% when enrolling participants in the medium- and high-risk tertiles, and 28–63% when enrolling participants in the high-risk tertile only (Fig. 6). The performance was comparable to that observed for the atrophy markers cortical thickness and grey matter volume (respectively 53% and 37% reductions when including participants in the high-risk tertile). Similar

Fig. 3: **Forest plots and spline plots for the associations of PVS and WML markers with dementia risk.** In two-stage pooled analyses that combined individual-participant data from three studies (Panels a–f), each additional 100 WM-PVS (Panel a) and 10 BG-PVS (Panel b) were associated with 20% and 8% decrease in dementia risk, each additional 0.1 mm increase in mean WM-PVS (Panel c) and BG-PVS (Panel d) diameter were associated with 8% and 15% increase in dementia risk, and each unit increase of the log-transformed P-WML volume (Panel e) was associated with 13% increase in dementia risk. Log-transformed D-WML volume (Panel f) was not associated with dementia risk. In each graph, the size of the squares indicates the weight given to the study, and the width of the diamond indicates the 95% confidence interval for the overall association estimate. Between-study heterogeneity was statistically assessed with the use of I^2. The spline analysis of pooled data (Panels g–l) supported a linear association over the range of WM-PVS count (Panel g; 2.5th–97.5th percentile, 206–762), BG-PVS count (Panel h; 2.5th–97.5th percentile, 71–244), WM-PVS diameter (Panel i; 2.5th–97.5th percentile, 1.77–2.30 mm), BG-PVS diameter (Panel j; 2.5th–97.5th percentile, 1.44–1.79) and P-WMH volume (Panel k; 2.5th–97.5th percentile, 0–9.1) within the overall population. Shaded areas indicate 95% confidence intervals, and the red line at 1.0 indicates the reference. Box plots at the bottom of the graphs show the distributions of the marker. The vertical bar indicates the median, and the ends of the box the interquartile range; the whiskers extend to values no farther than 1.5 times the interquartile range (which may be past the graphed area). P indicate P-values from the Cox models (panels a–f) and from the chi-square test for linearity (panels g–l). See also Supplementary Fig. S6 and Table S6 for sensitivity analysis. Data from three studies — the Alzheimer's Disease Neuroimaging Initiative (ADNI), the Open Access Series of Imaging Studies (OASIS), and the National Alzheimer's Coordinating Centre (NACC) — are shown. Hazard ratios were estimated from Cox models stratified according to study cohort with adjustment for age, sex, race, educational level, body mass index, CDR global score at the baseline, history of diabetes, cardio-/cerebro-vascular disease, hypertension, dyslipidaemia, family history of dementia, intracranial volume and the time interval between the MRI scan and the clinical visit of the cognitive assessment at the baseline.

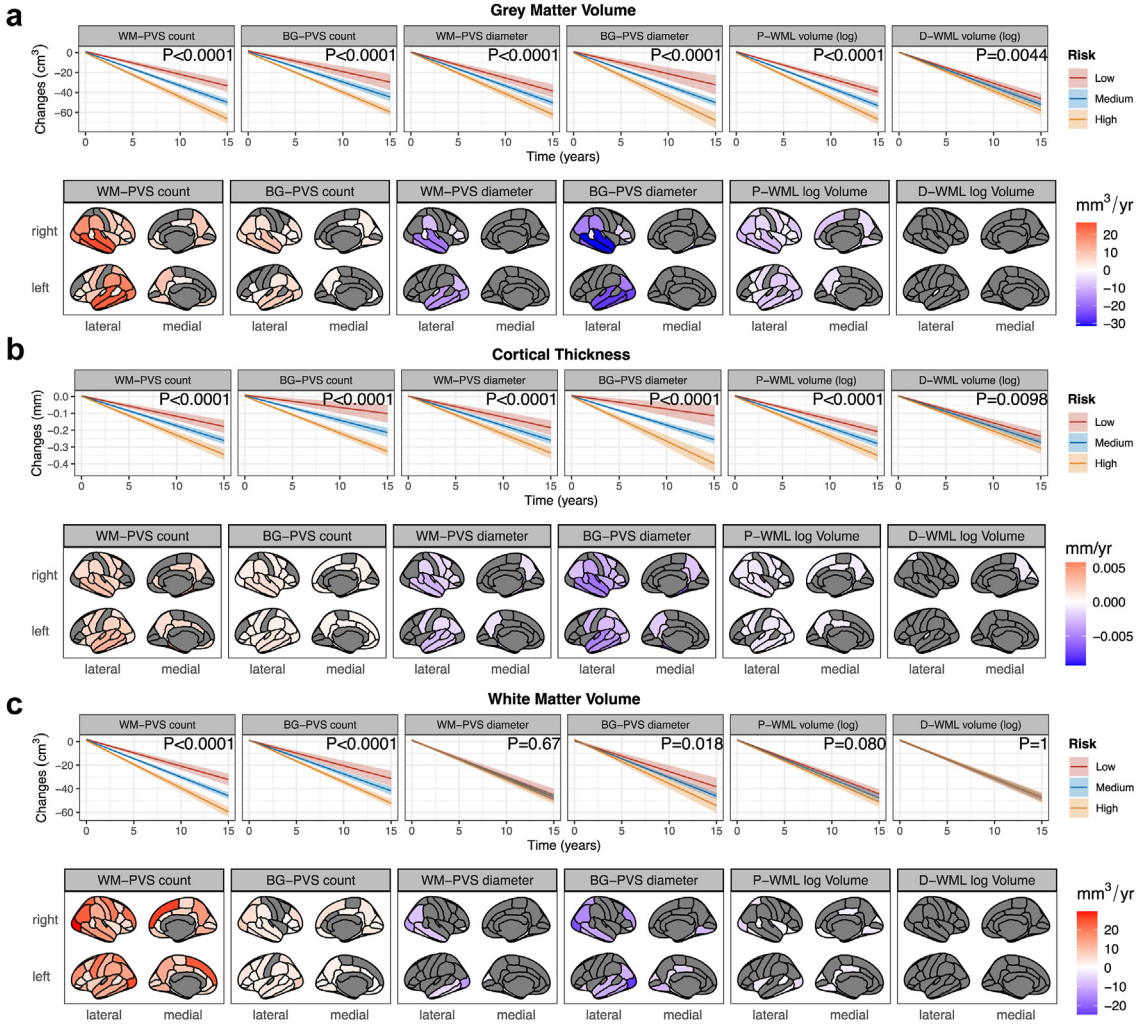

***Fig. 4:* Plots for the estimated trajectories of brain atrophy in relation to PVS and WML markers.** Top rows in each panel depict the effect of baseline PVS and WML markers on the trajectories of grey matter volume, cortical thickness, and white matter volume (Panels a–c, respectively). For each marker, equally spaced values from the low-risk (red), medium-risk (blue), and high-risk (yellow) tertile are shown (tertile limits in Supplementary Table S16). Shaded areas indicate 95% confidence intervals. P indicates adjusted significance value of the interaction term "marker" by "time" in linear mixed-effects models. The estimated volume or thickness preserved/lost per year for each additional unit increase in the marker are reported in Supplementary Table S8. The regional analysis (bottom rows in each panel) across cortical parcellations according to the Desikan-Killiany atlas reports the estimated volume or thickness preserved (positive values in red) or lost (negative values in blue) per year for each additional unit increase in the vascular marker. Only estimated values for regions that remained statistically significant after correction for multiple comparisons (68 comparisons) are shown; non-significant regions are greyed out. Coefficients for individual regions are reported in Supplementary Tables S9–S11 for grey matter volume, cortical thickness, and white matter volume, respectively. Estimates and corrected significance obtained from multivariable linear mixed-effects models with random intercepts and slopes for each individual participant (N = 3389 and 14,229 timepoints MRI scans). All models were adjusted for age, sex, race, educational level, body mass index, CDR global score at the baseline, history of diabetes, cardio-/cerebro-vascular disease, hypertension, dyslipidaemia, family history of dementia, intracranial volume, the baseline value of the dependent variable (grey matter volume, cortical thickness, or white matter volume), field strength, manufacturer, and intra-individual consistency of the protocol used for the longitudinal MRI acquisitions (consistent versus non-consistent protocol). See also Supplementary Figs. S10–S12 and Table S12 for sensitivity analysis.

results were obtained when the cognitive decline was assessed with MMSE (Supplementary Fig. S16) and when the trial length was set at 12- and 24-month (Supplementary Fig. S17a and b, respectively).

In multivariable models, medium- and high-risk tertiles for PVS markers were not significantly associated with amyloid-β or tau positive status (Supplementary Table S15), suggesting that screening participants

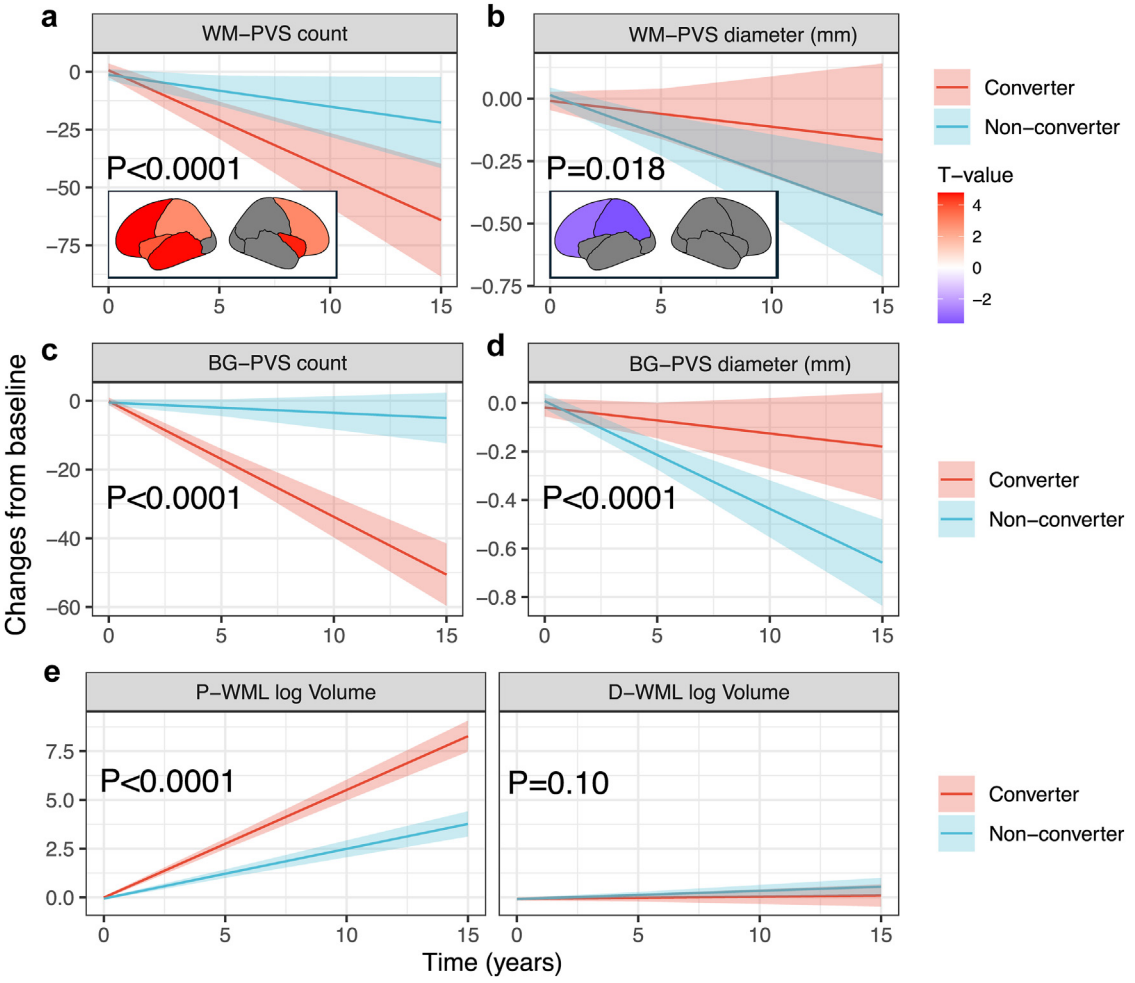

***Fig. 5:* Plots for the estimated longitudinal trajectories of PVS or WML markers according to conversion to dementia status.** Estimated longitudinal trajectories of WM-PVS (a–b), BG-PVS (c–d), and WML (e) markers for participants without dementia who converted to dementia (converters, red) and those that did not convert to dementia (non-converters, cyan). Trajectories are estimated from fully adjusted linear mixed-effect models; the adjusted P-values (P) indicate whether the trajectories are significantly different between converters and non-converters (interaction term "cognitive status" by "time" in linear mixed-effects models) after correction for multiple comparisons. Shaded areas indicate 95% confidence intervals. For WM-PVS markers (panels a–b), we estimated in each lobe of the left (L) and right (R) hemispheres the group-effect (expressed as T-value) for the longitudinal trajectories of the corresponding marker: positive values in red indicate significantly higher (i.e., less negative) slopes for non-converters versus converters, whereas negative values in blue indicate significantly lower (i.e., more negative) slopes for non-converters versus converters. Lobes where the longitudinal trajectories were not significantly different between converters and non-converters after correction for multiple comparisons are greyed-out. Estimates and corrected significance obtained from multivariable linear mixed-effects models with random intercepts and slopes for each individual participant (N = 3389 and 14,229 timepoints MRI scans). See also Supplementary Fig. S17 for sensitivity analysis.

without dementia according to our PVS markers is not linked to Alzheimer disease biomarkers. On the other hand, medium- and high-risk tertiles for P-WML volume, cortical thickness, and grey matter volume were associated with amyloid-β positive status (Supplementary Table S15).

Discussion

We developed a fully automated, robust algorithm to obtain unbiased, quantitative metrics of PVS from clinical brain MRI T1-weighted images. We demonstrated that our method provides accurate segmentations with high inter-scanner reproducibility. These characteristics allowed us to apply this algorithm to the brain MRI scans of 10,004 participants whose data were pooled from three publicly available studies performed in the United States and Canada. We found that after controlling for demographic and clinical covariates, lower PVS count and higher mean PVS diameter were significantly associated with a dose–response higher risk

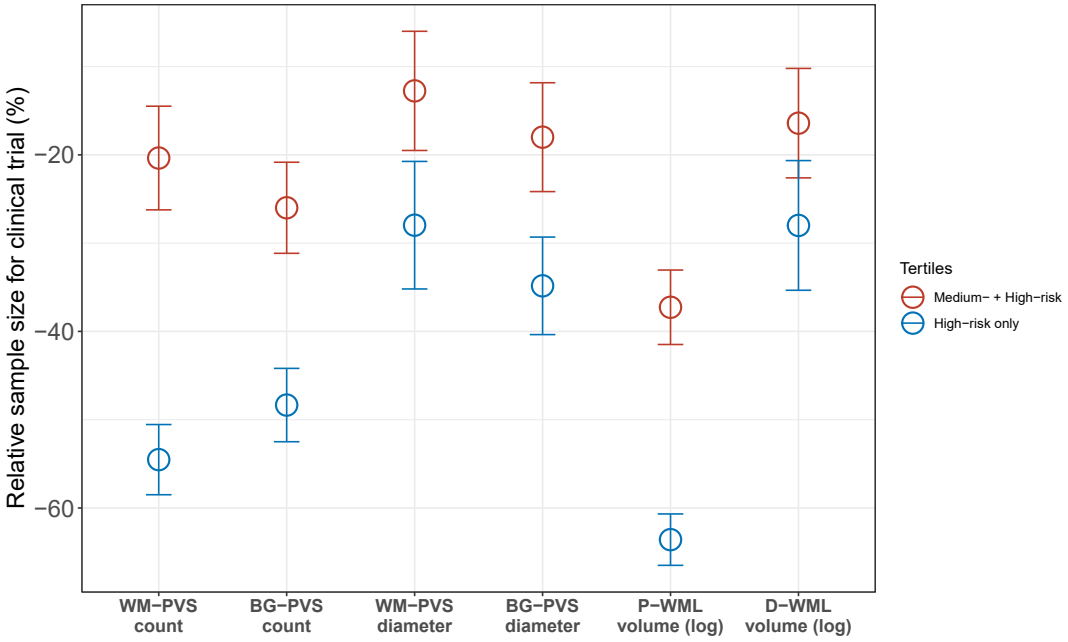

***Fig. 6:* Error-bar plot for the relative sample size in simulated clinical trials enriched using PVS or WML markers.** Relative sample sizes for simulated clinical trials in participants without dementia pooled from three studies (the Alzheimer's Disease Neuroimaging Initiative, the Open Access Series of Imaging Studies, and the National Alzheimer's Coordinating Centre). The simulations had statistical power of 80% at $\alpha = 0.05$ and assumed a 30% treatment effect for slopes in cognitive decline, 1:1 allocation of treatment, total trial length of 48 months, and outcome measures every 12 months. All available longitudinal cognitive data (40,307 cognitive assessments from 7518 participants without dementia) were used in these multivariable models. Mean relative sample sizes and the corresponding standard errors of the mean are across 500 bootstrap iterations. The reference model (without enrichment and with 100% inclusion) included all the tertiles. In the two enrichment models for each marker ("medium-risk + high-risk tertiles", red bars; "high-risk only tertile", blue bars), only participants in the indicated tertiles were included. Tertile limits for each marker are reported in Supplementary Table S16. See also Supplementary Figs. S18 and S19 for additional simulations.

of developing dementia, and with accelerated brain atrophy. The robustness and reliability of these results is related to the large sample size, the use of participant-level data and consistent approaches for covariate adjustments and modelling, and the consistency across multiple sensitivity analyses. These data show that PVS may represent a predictor of dementia.

Perivascular spaces represent a critical component of the glymphatic system, a system thought to be responsible for brain clearance of toxic and waste metabolites.[69] PVS are normally visible on MRI in all participants across the human lifespan,[47–49,70] including neonates,[71] and therefore they are not considered pathological markers *per se*.[9] However, changes to PVS structural and morphological features may be indicators of vascular-related pathology in the brain. A larger perivascular diameter for example might indicate alterations in the glymphatic flow and impairment of the clearance process, with subsequent accumulation of neurotoxic protein aggregates in the brain.[67,72,73] In our study, a larger PVS diameter at baseline predicted higher dementia risk and accelerated brain atrophy. Interestingly, PVS diameter remained larger over time in participants without dementia who developed dementia, indicating that the PVS enlargement occurs before the dementia status and that it may not increase indefinitely having reached a plateau. On the other hand, PVS diameter decreased with time in participants without dementia who remained dementia-free (non-converters), which could be related to a reduced cerebrospinal fluid production observed in healthy ageing.[74] In agreement with preclinical studies showing a relationship between glymphatic system and blood flow,[67,68] we found that PVS diameter was inversely correlated with cerebral blood flow. On the other hand, PVS count was positively correlated with brain perfusion, with a higher PVS count also associated with lower risk of dementia and slower brain atrophy. Since the PVS count obtained with our method included any MRI-visible PVS, regardless of whether they could be considered enlarged or not, we speculate that PVS count may be linked more to brain perfusion rather than to glymphatic dysfunction. A low PVS count might indicate cerebral hypoperfusion, a factor found associated with cognitive decline and brain atrophy.[75–78] Further studies specifically focused on cerebral perfusion are needed to better understand the

relationship between blood flow and PVS as well as their relative contribution to neurodegeneration and dementia.

The mechanisms underlying the pathophysiological alterations to the structure and function of PVS in the human brain remain poorly understood. Based on preclinical studies, it has been proposed that blood–brain barrier breakdown could result in the perivascular accumulation of blood-derived proteins/debris and subsequent dilation of the PVS.[79] Since the PVS visibility on MRI depends on the presence of cerebrospinal/interstitial fluid within the PVS,[9,79] the lower PVS count detected in participants at increased risk of dementia may arise from an early occlusion and/or obstruction of the PVS, resulting in loss of fluid signal and decreased detectability of PVS on MRI. Similarly, impaired clearance of brain metabolic waste products, including but not limited to amyloid-β, may also lead to their accumulation in the PVS,[79] with subsequent obstruction to the PVS fluid and loss of its signal on MRI (hence, lower PVS count). Finally, as previous studies showed that the fluid flow in PVS is driven by arterial pulsatility and vasomotion,[67,72,73,80–82] it is possible that arteriolosclerosis, which is typically observed in small vessel disease and is characterised by vessel wall rigidity, might reduce the fluid flow through PVS, with a subsequent redistribution of the PVS fluid resulting in: 1) enlargement of PVS where the stagnant fluid accumulated, and 2) lower amount of fluid in other PVS, which become less visible. Further studies are needed to better understand the pathophysiology of PVS structural alterations in the human brain.

Previous studies evaluating PVS and incident dementia performed manual visual assessment of perivascular spaces, a significant impediment for large studies and clinical trials, with serious concerns regarding inter- and intra-rater variability. This has led to mixed conclusions on the relationship between PVS and dementia. For example, previous meta-analyses investigated the relationship between WM-PVS and risk of dementia, but the results were conflicting, with significant heterogeneity between studies, variability in methods, and inconsistent adjustment for confounding factors.[1,83,84] Other studies in smaller cohorts also reported diverging results: some showed an association between perivascular space enlargement and higher risk of dementia,[85,86] while others found no increased risk[87] or increased risk of vascular dementia only.[88] Importantly, in all these studies the manual visual assessment included only the PVS that are more easily discernible to the human eye, i.e., those that are apparently enlarged, and prevented a quantitative analysis of the blood vessels with small/non-enlarged perivascular spaces, a limitation eliminated by our algorithm. Moreover, visual readings typically do not consider in their assessment the total intracranial volume, a factor strongly associated with PVS[9] and that we controlled for in all our models.

It should be noted that the PVS count assessed with our algorithm does not correspond to the PVS scores usually reported with traditional visual rating scales, because our algorithm 1) counts all PVS structures, regardless of their enlargement status, and 2) assesses PVS throughout the whole white matter and basal ganglia; visual scores instead are based only on a single slice and typically consider only enlarged PVS visible to the reader. On the other hand, the PVS mean diameter measured by our algorithm is a quantitative estimate of the degree of PVS enlargement overall.

Our MRI PVS markers required only a commonly acquired volumetric T1-weighted sequence, were computed in a fully-automated fashion, and showed excellent inter-scanner and test-retest reproducibility. These features may allow for our PVS markers to be readily implemented in clinical practice, as well as retrospective analyses of currently available brain MRI data. As we showed in our clinical trial simulations, their use may reduce the cost and duration of clinical trials for dementia prevention and treatment by facilitating the identification and enrolment of participants with increased risk of cognitive decline. Indeed, we found that after screening out participants based on our PVS markers, there was a substantial reduction in the minimal number of participants required for detecting the intervention effect, suggesting an increase in the power of the trial. Importantly, medium and high-risk tertiles of our PVS markers were not linked to positive amyloid-β and tau status, in contrast with WML and atrophy markers, indicating that the selection of participants based on our PVS markers is independent of Alzheimer disease biomarker status. In the case of trials for treatments specifically targeting Alzheimer disease hallmark pathology such as amyloid-β and tau (i.e., enrolling participants positive for amyloid-β and/or tau), these PVS markers would allow to identify and exclude people at high risk of vascular/perivascular co-pathology, enhancing the trial for a more homogenous cohort of preclinical Alzheimer disease. Early detection of an increased risk of dementia could also motivate patients to adopt healthy lifestyle modifications, encouraging healthcare professionals to implement preventive measures and initiate timely treatments and support, thereby improving patient and family member quality of life. Finally, these MRI markers open new opportunities to robustly investigate perivascular spaces *in vivo* in a variety of other neurological conditions and treatment paradigms, allowing to potentially identify subtle cerebrovascular damages and to gain new insights on the human brain vasculature and glymphatics.

We acknowledge the following limitations in our study. First, our analytic approach allowed us to reduce the degree of heterogeneity across studies, but some heterogeneity remained, intrinsic to the original study design, such as the health profile of participants and availability and type of information on covariates.

Despite the excellent inter-scanner reproducibility of our PVS markers, we cannot exclude that differences in the MRI scanner and acquisition protocols might still in part influence the estimation of PVS/WML markers. Importantly, the inter-study heterogeneity estimation may be inaccurate due to the low number of studies assessed in the meta-analysis. Another important limitation is the inability to assess the potential role of residual unmeasured confounding factors, such as diet and socioeconomic status, which were not available in the analysed databases. Third, the built-in selection bias in the hazard ratios[89] may lead to inaccurate estimation of the risk and distorted inferences. Fourth, as we were restricted to populations recruited by the original studies, our cohort comprised mainly white participants, and increased representation of other racial and ethnic groups would be critical to generalization. Fifth, we cannot exclude that small lesions with vascular shape may be included in our PVS segmentation masks. Nevertheless, the influence of these potential lesions to our statistical analyses may be considered negligible, since even a few lesions in a single participant would represent a very small proportion of the total PVS count estimated in that participant (interquartile range of WM-PVS and BG-PVS per participant in our study were 339–530 and 106–166, respectively). Finally, we could not discriminate whether our PVS metrics refer to periarteriolar or perivenous compartment. However, previous studies have shown that the majority of the MRI-visible PVS overlap with arterioles,[90–93] therefore it is reasonable to assume that the PVS metrics in our analysis refer mostly to arterioles and their periarteriolar compartment.

In conclusion, using our fully-automated, robust algorithm for assessing perivascular spaces in the cerebral white matter and basal ganglia, we found a significant linear association of low PVS count and high PVS diameter with increased risk of dementia and accelerated brain atrophy. Baseline values and longitudinal trajectories of PVS metrics were significantly different in participants without dementia who converted to dementia compared with non-converters. These results support a link between PVS and cognitive impairment, opening new opportunities to risk-stratify participants for clinical trial enrolment, early healthcare interventions to combat dementia, and accelerated research in human brain glymphatics.

Contributors

Conceptualisation: Giuseppe Barisano, Jeiran Choupan and Melanie Hayden-Gephart.
Data curation: Giuseppe Barisano.
Formal analysis: Giuseppe Barisano.
Funding acquisition: Jeiran Choupan and Melanie Hayden-Gephart.
Investigation: All authors.
Software: Giuseppe Barisano.
Supervision: Jeiran Choupan and Melanie Hayden-Gephart.
Visualisation: Giuseppe Barisano.
Writing–original draft: Giuseppe Barisano.
Writing–review & editing: All authors.

Giuseppe Barisano, Jeiran Choupan and Melanie Hayden-Gephart had access and verified the underlying data.

All authors read and approved the final version of the manuscript. Data used in preparation of this article were obtained from the Alzheimer's Disease Neuroimaging Initiative (ADNI) database (adni.loni.usc.edu). As such, the investigators within the ADNI provided MRI and clinical data but did not participate in analysis or writing of this report.

Data sharing statement

Requests for clinical information and MRI data should be submitted to ADNI (https://adni.loni.usc.edu/), NACC (https://naccdata.org/), and OASIS (https://www.oasis-brains.org/). Perivascular spaces (PVS) segmentation masks and data are available at https://gbarisano.shinyapps.io/pvs-dementia/.

Declaration of interests

Giuseppe Barisano is listed as inventor on a patent application related to this work filed by Stanford University. The other authors declare that they have no competing interests.

Data collection and sharing for this project was funded by the Alzheimer's Disease Neuroimaging Initiative (ADNI) (National Institutes of Health Grant U01 AG024904) and DOD ADNI (Department of Defense award number W81XWH-12-2-0012). ADNI is funded by the National Institute on Ageing, the National Institute of Biomedical Imaging and Bioengineering, and through generous contributions from the following: AbbVie, Alzheimer's Association; Alzheimer's Drug Discovery Foundation; Araclon Biotech; BioClinica, Inc.; Biogen; Bristol-Myers Squibb Company; CereSpir, Inc.; Cogstate; Eisai Inc.; Elan Pharmaceuticals, Inc.; Eli Lilly and Company; EuroImmun; F. Hoffmann-La Roche Ltd and its affiliated company Genentech, Inc.; Fujirebio; GE Healthcare; IXICO Ltd.; Janssen Alzheimer Immunotherapy Research & Development, LLC.; Johnson & Johnson Pharmaceutical Research & Development LLC.; Lumosity; Lundbeck; Merck & Co., Inc.; Meso Scale Diagnostics, LLC.; NeuroRx Research; Neurotrack Technologies; Novartis Pharmaceuticals Corporation; Pfizer Inc.; Piramal Imaging; Servier; Takeda Pharmaceutical Company; and Transition Therapeutics. The Canadian Institutes of Health Research is providing funds to support ADNI clinical sites in Canada. Private sector contributions are facilitated by the Foundation for the National Institutes of Health (www.fnih.org). The grantee organization is the Northern California Institute for Research and Education, and the study is coordinated by the Alzheimer's Therapeutic Research Institute at the University of Southern California. ADNI data are disseminated by the Laboratory for Neuro Imaging at the University of Southern California.

Acknowledgements

The authors thank all the participants and personnel involved in the data collection.

The authors G.B. and M.H. are supported by a grant (U54CA261717to Dr. Hayden-Gephart) from the National Institutes of Health (NIH), J.C. is supported by grants RF1MH123223, R01AG070825, and R01NS128486 from the NIH.

The authors thank Dr. Michael Greicius, M.D., from the Department of Neurology at Stanford University for valuable discussion of the manuscript.

The image computing resources provided by the Laboratory of Neuro Imaging Resource (LONIR) at the University of Southern California are supported in part by NIH National Institute of Biomedical Imaging and Bioengineering (NIBIB) grant P41EB015922.

Data used in preparation of this article include data obtained from the MarkVCID consortium. A complete listing of MarkVCID investigators can be found at: www.markvcid.org.

ADNI: Data collection and sharing for this project was funded by the Alzheimer's Disease Neuroimaging Initiative (ADNI) (National Institutes of Health Grant U01 AG024904) and DOD ADNI (Department of Defense award number W81XWH-12-2-0012). ADNI is funded by the National Institute on Ageing, the National Institute of Biomedical

Imaging and Bioengineering, and through generous contributions from the following: AbbVie, Alzheimer's Association; Alzheimer's Drug Discovery Foundation; Araclon Biotech; BioClinica, Inc.; Biogen; Bristol-Myers Squibb Company; CereSpir, Inc.; Cogstate; Eisai Inc.; Elan Pharmaceuticals, Inc.; Eli Lilly and Company; EuroImmun; F. Hoffmann-La Roche Ltd and its affiliated company Genentech, Inc.; Fujirebio; GE Healthcare; IXICO; Janssen Alzheimer Immunotherapy Research & Development, LLC.; Johnson & Johnson Pharmaceutical Research & Development LLC.; Lumosity; Lundbeck; Merck & Co., Inc.; Meso Scale Diagnostics, LLC.; NeuroRx Research; Neurotrack Technologies; Novartis Pharmaceuticals Corporation; Pfizer Inc.; Piramal Imaging; Servier; Takeda Pharmaceutical Company; and Transition Therapeutics. The Canadian Institutes of Health Research is providing funds to support ADNI clinical sites in Canada. Private sector contributions are facilitated by the Foundation for the National Institutes of Health (www.fnih.org). The grantee organization is the Northern California Institute for Research and Education, and the study is coordinated by the Alzheimer's Therapeutic Research Institute at the University of Southern California. ADNI data are disseminated by the Laboratory for Neuro Imaging at the University of Southern California.

NACC: The National Alzheimer's Coordinating Centre (NACC) database is funded by NIA/NIH Grant U24 AG072122. NACC data are contributed by the NIA-funded ADRCs: P30 AG062429 (PI James Brewer, MD, PhD), P30 AG066468 (PI Oscar Lopez, MD), P30 AG062421 (PI Bradley Hyman, MD, PhD), P30 AG066509 (PI Thomas Grabowski, MD), P30 AG066514 (PI Mary Sano, PhD), P30 AG066530 (PI Helena Chui, MD), P30 AG066507 (PI Marilyn Albert, PhD), P30 AG066444 (PI John Morris, MD), P30 AG066518 (PI Jeffrey Kaye, MD), P30 AG066512 (PI Thomas Wisniewski, MD), P30 AG066462 (PI Scott Small, MD), P30 AG072979 (PI David Wolk, MD), P30 AG072972 (PI Charles DeCarli, MD), P30 AG072976 (PI Andrew Saykin, PsyD), P30 AG072975 (PI David Bennett, MD), P30 AG072978 (PI Neil Kowall, MD), P30 AG072977 (PI Robert Vassar, PhD), P30 AG066519 (PI Frank LaFerla, PhD), P30 AG062677 (PI Ronald Petersen, MD, PhD), P30 AG079280 (PI Eric Reiman, MD), P30 AG062422 (PI Gil Rabinovici, MD), P30 AG066511 (PI Allan Levey, MD, PhD), P30 AG072946 (PI Linda Van Eldik, PhD), P30 AG062715 (PI Sanjay Asthana, MD, FRCP), P30 AG072973 (PI Russell Swerdlow, MD), P30 AG066506 (PI Todd Golde, MD, PhD), P30 AG066508 (PI Stephen Strittmatter, MD, PhD), P30 AG066515 (PI Victor Henderson, MD, MS), P30 AG072947 (PI Suzanne Craft, PhD), P30 AG072931 (PI Henry Paulson, MD, PhD), P30 AG066546 (PI Sudha Seshadri, MD), P20 AG068024 (PI Erik Roberson, MD, PhD), P20 AG068053 (PI Justin Miller, PhD), P20 AG068077 (PI Gary Rosenberg, MD), P20 AG068082 (PI Angela Jefferson, PhD), P30 AG072958 (PI Heather Whitson, MD), P30 AG072959 (PI James Leverenz, MD).

OASIS: Data were provided in part by the Open Access Series of Imaging Studies (OASIS) OASIS-3: Longitudinal Multimodal Neuroimaging: Principal Investigators: T. Benzinger, D. Marcus, J. Morris; NIH P30 AG066444, P50 AG00561, P30 NS09857781, P01 AG026276, P01 AG003991, R01 AG043434, UL1 TR000448, R01 EB009352, NIH P30 AG066444, AW00006993.

AV-45 doses were provided by Avid Radiopharmaceuticals, a wholly owned subsidiary of Eli Lilly.

AV-1451 doses were provided by Avid Radiopharmaceuticals, a wholly owned subsidiary of Eli Lilly.

MarkVCID: MarkVCID was launched in 2016 by the NIH's National Institute of Neurological Disorders and Stroke (NINDS) and National Institute on Ageing (NIA), and consists of research groups across the United States. The primary goal of MarkVCID is to generate a suite of validated biomarkers ready for application to clinical trials aimed at identifying disease-modifying therapies for VCID. For up-to-date information, see www.markvcid.org. Data collection and sharing was funded by NINDS/NIA as part of the Biomarkers Consortium for Vascular Contributions to Cognitive Impairment and Dementia (MarkVCID): U24NS100591, UH2NS100599, UH2NS100605, UH2NS100588, UH2NS100608, UH2NS100606, UH2NS100598, UH2NS100614.

Human Connectome Project: Data were provided in part by the Human Connectome Project (HCP), WU-Minn Consortium (1U54MH091657) funded by the 16 NIH Institutes and Centres that support the NIH Blueprint for Neuroscience Research; and by the McDonnell Centre for Systems Neuroscience at Washington University. Data from HCP-Ageing cohort was supported by the National Institute on Ageing of the National Institutes of Health under Award Number U01AG052564. Data from HCP-Development cohort was supported by the National Institute of Mental Health of the National Institutes of Health under Award Number U01MH109589. The content is solely the responsibility of the authors and does not necessarily represent the official views of the National Institutes of Health. MRI and clinical data can be accessed from https://www.humanconnectome.org.

Members of the Alzheimer's Disease Neuroimaging Initiative: Michael Weiner, Paul Aisen, Ronald Petersen, Clifford R. Jack, William Jagust, John Q. Trojanowki, Arthur W. Toga, Laurel Beckett, Robert C. Green, Andrew J. Saykin, John Morris, Leslie M. Shaw, Enchi Liu, Tom Montine, Ronald G. Thomas, Michael Donohue, Sarah Walter, Devon Gessert, Tamie Sather, Gus Jiminez, Danielle Harvey, Michael Donohue, Matthew Bernstein, Nick Fox, Paul Thompson, Norbert Schuff, Charles DeCarli, Bret Borowski, Jeff Gunter, Matt Senjem, Prashanthi Vemuri, David Jones, Kejal Kantarci, Chad Ward, Robert A. Koeppe, Norm Foster, Eric M. Reiman, Kewei Chen, Chet Mathis, Susan Landau, Nigel J. Cairns, Erin Householder, Lisa Taylor Reinwald, Virginia Lee, Magdalena Korecka, Michal Figurski, Karen Crawford, Scott Neu, Tatiana M. Foroud, Steven Potkin, Li Shen, Faber Kelley, Sungeun Kim, Kwangsik Nho, Zaven Kachaturian, Richard Frank, Peter J. Snyder, Susan Molchan, Jeffrey Kaye, Joseph Quinn, Betty Lind, Raina Carter, Sara Dolen, Lon S. Schneider, Sonia Pawluczyk, Mauricio Beccera, Liberty Teodoro, Bryan M. Spann, James Brewer, Helen Vanderswag, Adam Fleisher, Judith L. Heidebrink, Joanne L. Lord, Ronald Petersen, Sara S. Mason, Colleen S. Albers, David Knopman, Kris Johnson, Rachelle S. Doody, Javier Villanueva Meyer, Munir Chowdhury, Susan Rountree, Mimi Dang, Yaakov Stern, Lawrence S. Honig, Karen L. Bell, Beau Ances, John C. Morris, Maria Carroll, Sue Leon, Erin Householder, Mark A. Mintun, Stacy Schneider, Angela Oliver, Daniel Marson, Randall Griffith, David Clark, David Geld-macher, John Brockington, Erik Roberson, Hillel Grossman, Effie Mitsis, Leyla deToledo-Morrell, Raj C. Shah, Ranjan Duara, Daniel Varon, Maria T. Greig, Peggy Roberts, Marilyn Albert, Chiadi Onyike, Daniel D'Agostino, Stephanie Kielb, James E. Galvin, Dana M. Pogorelec, Brittany Cerbone, Christina A. Michel, Henry Rusinek, Mony J. de Leon, Lidia Glodzik, Susan De Santi, P. Murali Doraiswamy, Jeffrey R. Petrella, Terence Z. Wong, Steven E. Arnold, Jason H. Karlawish, David Wolk, Charles D. Smith, Greg Jicha, Peter Hardy, Partha Sinha, Elizabeth Oates, Gary Conrad, Oscar L. Lopez, MaryAnn Oakley, Donna M. Simpson, Anton P. Porsteinsson, Bonnie S. Goldstein, Kim Martin, Kelly M. Makino, M. Saleem Ismail, Connie Brand, Ruth A. Mulnard, Gaby Thai, Catherine Mc Adams Ortiz, Kyle Womack, Dana Mathews, Mary Quiceno, Ramon Diaz Arrastia, Richard King, Myron Weiner, Kristen Martin Cook, Michael DeVous, Allan I. Levey, James J. Lah, Janet S. Cellar, Jeffrey M. Burns, Heather S.Anderson, Russell H. Swerdlow, Liana Apostolova, Kathleen Tingus, Ellen Woo, Daniel H.S. Silverman, Po H. Lu, George Bartzokis, Neill R Graff Radford, Francine Parfitt, Tracy Kendall, Heather Johnson, Martin R. Farlow, AnnMarie Hake, Brandy R. Matthews, Scott Herring, Cynthia Hunt, Christopher H. van Dyck, Richard E. Carson, Martha G. MacAvoy, Howard Chertkow, Howard Bergman, Chris Hosein, Sandra Black, Bojana Stefanovic, Curtis Caldwell, Ging-Yuek Robin Hsiung, Howard Feldman, Benita Mudge, Michele Assaly, Andrew Kertesz, John Rogers, Dick Trost, Charles Bernick, Donna Munic, Diana Kerwin, Marek Marsel Mesulam, Kristine Lipowski, Chuang Kuo Wu, Nancy Johnson, Carl Sadowsky, Walter Martinez, Teresa Villena, Raymond Scott Turner, Kathleen Johnson, Brigid Reynolds, Reisa A. Sperling, Keith A. Johnson, Gad Marshall, Meghan Frey, Jerome Yesavage, Joy L. Taylor, Barton Lane, Allyson Rosen, Jared Tinklenberg, Marwan N. Sabbagh, Christine M. Belden, Sandra A. Jacobson, Sherye A. Sirrel, Neil Kowall, Ronald Killiany, Andrew E. Budson, Alexander Norbash, Patricia Lynn Johnson, Thomas O. Obisesan, Saba Wolday, Joanne Allard, Alan Lerner, Paula

Ogrocki, Leon Hudson, Evan Fletcher, Owen Carmichael, John Olichney, Charles DeCarli, Smita Kittur, Michael Borrie, TY Lee, Rob Bartha, Sterling Johnson, Sanjay Asthana, Cynthia M. Carlsson, Steven G. Potkin, Adrian Preda, Dana Nguyen, Pierre Tariot, Adam Fleisher, Stephanie Reeder, Vernice Bates, Horacio Capote, Michelle Rainka, Douglas W. Scharre, Maria Kataki, Anahita Adeli, Earl A. Zimmerman, Dzintra Celmins, Alice D. Brown, Godfrey D. Pearlson, Karen Blank, Karen Anderson, Robert B. Santulli, Tamar J. Kitzmiller, Eben S.Schwartz, Kaycee M. Sink, Jeff D. Williamson, Pradeep Garg, Franklin Watkins, Brian R. Ott, Henry Querfurth, Geoffrey Tremont, Stephen Salloway, Paul Malloy, Stephen Correia, Howard J. Rosen, Bruce L. Miller, Jacobo Mintzer, Kenneth Spicer, David Bachman, Elizabeth Finger, Stephen Pasternak, Irina Rachinsky, John Rogers, Andrew Kertesz, Dick Drost, Nunzio Pomara, Raymundo Hernando, Antero Sarrael, Susan K. Schultz, Laura L. Boles Ponto, Hyungsub Shim, Karen Elizabeth Smith, Norman Relkin, Gloria Chaing, Lisa Raudin, Amanda Smith, Kristin Fargher, Balebail Ashok Raj.

Appendix A. Supplementary data

Supplementary data related to this article can be found at https://doi.org/10.1016/j.ebiom.2024.105523.

References

1 Debette S, Schilling S, Duperron MG, Larsson SC, Markus HS. Clinical significance of magnetic resonance imaging markers of vascular brain injury: a systematic review and meta-analysis. *JAMA Neurol*. 2018;76(1):81–94.

2 Wardlaw JM, Smith C, Dichgans M. Small vessel disease: mechanisms and clinical implications. *Lancet Neurol*. 2019;18(7):684–696 [cited 2020 Jun 26]; Available from: https://pubmed-ncbi-nlm-nih-gov.libproxy2.usc.edu/31097385/.

3 Arvanitakis Z, Capuano AW, Leurgans SE, Bennett DA, Schneider JA. Relation of cerebral vessel disease to Alzheimer's disease dementia and cognitive function in elderly people: a cross-sectional study. *Lancet Neurol*. 2016;15(9):934–943 [cited 2020 Jun 30]; Available from: https://pubmed-ncbi-nlm-nih-gov.libproxy2.usc.edu/27312738/.

4 Roher AE, Tyas SL, Maarouf CL, et al. Intracranial atherosclerosis as a contributing factor to Alzheimer's disease dementia. *Alzheimers Dement*. 2011;7(4):436 [cited 2023 Nov 7];Available from: /pmc/articles/PMC3117084/.

5 Dolan H, Crain B, Troncoso J, Resnick SM, Zonderman AB, Obrien RJ. Atherosclerosis, dementia, and alzheimer disease in the Baltimore longitudinal study of aging cohort. *Ann Neurol*. 2010;68(2):231–240 [cited 2023 Nov 7]; Available from: https://pubmed.ncbi.nlm.nih.gov/20695015/.

6 Fu C, Chute DJ, Farag ES, Garakian J, Cummings JL, Vinters HV. Comorbidity in dementia: an autopsy study. *Arch Pathol Lab Med*. 2004;128(1):32–38 [cited 2023 Nov 7]; Available from: https://pubmed.ncbi.nlm.nih.gov/14692815/.

7 Beach TG, Wilson JR, Sue LI, et al. Circle of Willis atherosclerosis: association with Alzheimer's disease, neuritic plaques and neurofibrillary tangles. *Acta Neuropathol*. 2007;113(1):13–21 [cited 2023 Nov 7]; Available from: https://pubmed.ncbi.nlm.nih.gov/17021755/.

8 Duering M, Biessels GJ, Brodtmann A, et al. Neuroimaging standards for research into small vessel disease—advances since 2013. *Lancet Neurol*. 2023;22(7):602–618 [cited 2023 Jun 5]; Available from: http://www.ncbi.nlm.nih.gov/pubmed/37236211.

9 Barisano G, Lynch KM, Sibilia F, et al. Imaging perivascular space structure and function using brain MRI. *Neuroimage*. 2022;257:119329 [cited 2022 May 23]; Available from: https://linkinghub.elsevier.com/retrieve/pii/S1053811922004487.

10 Schwartz DL, Boespflug EL, Lahna DL, Pollock J, Roese NE, Silbert LC. Autoidentification of perivascular spaces in white matter using clinical field strength T1 and FLAIR MR imaging. *Neuroimage*. 2019;202 [cited 2024 Feb 20]; Available from: https://pubmed.ncbi.nlm.nih.gov/31461676/.

11 Rashid T, Liu H, Ware JB, et al. Deep learning based detection of enlarged perivascular spaces on brain MRI. *Neuroimage Reports*. 2023;3(1) [cited 2024 Feb 20]; Available from: https://pubmed.ncbi.nlm.nih.gov/37035520/.

12 Sepehrband F, Barisano G, Sheikh-Bahaei N, et al. Image processing approaches to enhance perivascular space visibility and quantification using MRI. *Sci Rep*. 2019;9(1):12351 [cited 2019 Aug 26]; Available from: http://www.nature.com/articles/s41598-019-48910-x.

13 Ballerini L, Lovreglio R, Valdés Hernández MDC, et al. Perivascular spaces segmentation in brain MRI using optimal 3D filtering. *Sci Rep*. 2018;8(1):1–11.

14 Ramirez J, Berezuk C, McNeely AA, Gao F, McLaurin J, Black SE. Imaging the perivascular space as a potential biomarker of neurovascular and neurodegenerative diseases. *Cell Mol Neurobiol*. 2016;36(2):289–299 [cited 2017 Sep 28]; Available from: http://link.springer.com/10.1007/s10571-016-0343-6.

15 Boespflug EL, Schwartz DL, Lahna D, et al. MR imaging–based multimodal autoidentification of perivascular spaces (mMAPS): automated morphologic segmentation of enlarged perivascular spaces at clinical field strength. *Radiology*. 2018;286(2):632–642. Available from: http://pubs.rsna.org/doi/10.1148/radiol.2017170205.

16 Frangi AF, Niessen WJ, Vincken KL, Viergever MA. Multiscale vessel enhancement filtering. In: *Medical image computing and computer-assisted intervention— Miccai'98 1496*. Berlin, Heidelberg: Springer; 1998:130–137 [cited 2017 Sep 25]. Available from: http://link.springer.com/10.1007/BFb0056195.

17 Sepehrband F, Barisano G, Sheikh-Bahaei N, et al. Volumetric distribution of perivascular space in relation to mild cognitive impairment. *Neurobiol Aging*. 2021;99:28–43 [cited 2020 Dec 17]; Available from: https://linkinghub.elsevier.com/retrieve/pii/S0197458020304218.

18 Caprihan A, Hillmer L, Erhardt EB, et al. A trichotomy method for defining homogeneous subgroups in a dementia population. *Ann Clin Transl Neurol*. 2023;10(10):1802–1815 [cited 2023 Nov 6]; Available from: https://onlinelibrary.wiley.com/doi/full/10.1002/acn3.51869.

19 Vernooij MW, Pizzini FB, Schmidt R, et al. Dementia imaging in clinical practice: a European-wide survey of 193 centres and conclusions by the ESNR working group. *Neuroradiology*. 2019;61(6):633–642 [cited 2024 Mar 20]; Available from: https://link.springer.com/article/10.1007/s00234-019-02188-y.

20 Insel PS, Weiner M, Scott MacKin R, et al. Determining clinically meaningful decline in preclinical Alzheimer disease. *Neurology*. 2019;93(4):E322–E333 [cited 2023 Dec 1]; Available from: https://pubmed.ncbi.nlm.nih.gov/31289148/.

21 Weiner MW, Veitch DP, Aisen PS, et al. *The Alzheimer's Disease Neuroimaging Initiative 3: continued innovation for clinical trial improvement*. Alzheimer's and Dementia Elsevier Inc.; 2017:561–571.

22 Beekly DL, Ramos EM, Lee WW, et al. The National Alzheimer's Coordinating Center (NACC) database: the uniform data set. *Alzheimer Dis Assoc Disord*. 2007;21(3):249–258.

23 LaMontagne PJ, Benzinger TL, Morris JC, et al. OASIS-3: longitudinal neuroimaging, clinical, and cognitive dataset for normal aging and alzheimer disease. *medRxiv*; 2019, 2019.12.13.19014902. [cited 2023 Nov 10]; Available from: https://www.medrxiv.org/content/10.1101/2019.12.13.19014902v1.

24 Petersen RC, Aisen PS, Beckett LA, et al. Alzheimer's disease neuroimaging initiative (ADNI): clinical characterization. *Neurology*. 2010;74(3):201 [cited 2023 Dec 20];Available from: /pmc/articles/PMC2809036/.

25 Hachinski VC, Iliff LD, Zilhka E, et al. Cerebral blood flow in dementia. *Arch Neurol*. 1975;32(9):632–637 [cited 2023 Dec 20]; Available from: https://jamanetwork.com/journals/jamaneurology/fullarticle/573931.

26 Yesavage JA, Brink TL, Rose TL, et al. Development and validation of a geriatric depression screening scale: a preliminary report. *J Psychiatr Res*. 1982;17(1):37–49 [cited 2023 Dec 20]; Available from: https://pubmed.ncbi.nlm.nih.gov/7183759/.

27 Budelier MM, Bateman RJ. Biomarkers of alzheimer disease. *J Appl Lab Med*. 2020;5(1):194 [cited 2023 Oct 28];Available from: /pmc/articles/PMC7246147/.

28 Landau SM, Mintun MA, Joshi AD, et al. Amyloid deposition, hypometabolism, and longitudinal cognitive decline. *Ann Neurol*. 2012;72(4):578–586 [cited 2024 Jan 11]; Available from: https://onlinelibrary.wiley.com/doi/full/10.1002/ana.23650.

29 Royse SK, Minhas DS, Lopresti BJ, et al. Validation of amyloid PET positivity thresholds in centiloids: a multisite PET study approach. *Alzheimer's Res Ther*. 2021;13(1):1–10 [cited 2024 Jan 14]; Available from: https://alzres.biomedcentral.com/articles/10.1186/s13195-021-00836-1.

30 Jagust WJ, Bandy D, Chen K, et al. The Alzheimer's Disease Neuroimaging Initiative positron emission tomography core.

Alzheimer's Dement. 2010;6(3):221–229 [cited 2024 Jan 11];Available from: /pmc/articles/PMC2920531/.
31 Fagan AM, Shaw LM, Xiong C, et al. Comparison of analytical platforms for cerebrospinal fluid measures of Aβ1-42, total tau and p-tau181 for identifying Alzheimer's disease amyloid plaque pathology. *Arch Neurol*. 2011;68(9):1137 [cited 2023 Oct 28];Available from: /pmc/articles/PMC3154969/.
32 Shaw LM, Vanderstichele H, Knapik-Czajka M, et al. Cerebrospinal fluid biomarker signature in alzheimer's disease neuroimaging initiative subjects. *Ann Neurol*. 2009;65(4):403 [cited 2023 Oct 30];Available from: /pmc/articles/PMC2696350/.
33 Chappell MA, Groves AR, Whitcher B, Woolrich MW. Variational Bayesian inference for a nonlinear forward model. *IEEE Trans Signal Process*. 2009;57(1):223–236.
34 Chappell MA, Groves AR, MacIntosh BJ, Donahue MJ, Jezzard P, Woolrich MW. Partial volume correction of multiple inversion time arterial spin labeling MRI data. *Magn Reson Med*. 2011;65(4):1173–1183 [cited 2024 Jun 28]; Available from: https://onlinelibrary.wiley.com/doi/full/10.1002/mrm.22641.
35 Morris JC. The clinical dementia rating (CDR). *Neurology*. 1993;43(11):2412.2, 2412-a. Available from: https://www.neurology.org/lookup/doi/10.1212/WNL.43.11.2412-a.
36 Folstein MF, Folstein SE, McHugh PR. "Mini-mental state". A practical method for grading the cognitive state of patients for the clinician. *J Psychiatr Res*. 1975;12(3):189–198 [cited 2023 Nov 10]; Available from: https://pubmed.ncbi.nlm.nih.gov/1202204/.
37 McKhann GM, Knopman DS, Chertkow H, et al. The diagnosis of dementia due to Alzheimer's disease: recommendations from the National Institute on Aging-Alzheimer's Association workgroups on diagnostic guidelines for Alzheimer's disease. *Alzheimer's Dement*. 2011;7(3):263–269 [cited 2017 Oct 9]; Available from: https://onlinelibrary.wiley.com/doi/10.1016/j.jalz.2011.03.005.
38 McKhann G, Drachman D, Folstein M, Katzman R, Price D, Stadlan EM. Clinical diagnosis of alzheimer's disease: report of the NINCDS-ADRDA work group★ under the auspices of department of health and human services task force on alzheimer's disease. *Neurology*. 1984;34(7):939–944 [cited 2020 Aug 3]; Available from: https://pubmed-ncbi-nlm-nih-gov.libproxy2.usc.edu/6610841/.
39 Fischl B. FreeSurfer. *Neuroimage*. 2012;62(2):774–781 [cited 2019 Dec 16]; Available from: http://www.ncbi.nlm.nih.gov/pubmed/22248573.
40 Reuter M, Schmansky NJ, Rosas HD, Fischl B. Within-subject template estimation for unbiased longitudinal image analysis. *Neuroimage*. 2012;61(4):1402–1418.
41 Puonti O, Iglesias JE, Van Leemput K. Fast and sequence-adaptive whole-brain segmentation using parametric Bayesian modeling. *Neuroimage*. 2016;143:235–249.
42 Barisano G, Sepehrband F, Collins HR, et al. The effect of prolonged spaceflight on cerebrospinal fluid and perivascular spaces of astronauts and cosmonauts. *Proc Natl Acad Sci USA*. 2022;119(17):e2120439119 [cited 2022 Apr 13]; Available from: https://pubmed-ncbi-nlm-nih-gov.libproxy2.usc.edu/35412862/.
43 Wilcock D, Jicha G, Blacker D, et al. MarkVCID cerebral small vessel consortium: I. Enrollment, clinical, fluid protocols. *Alzheimers Dement*. 2021;17(4):704–715 [cited 2023 Nov 21]; Available from: https://pubmed.ncbi.nlm.nih.gov/33480172/.
44 Somerville LH, Bookheimer SY, Buckner RL, et al. The Lifespan Human Connectome Project in Development: a large-scale study of brain connectivity development in 5–21 year olds. *Neuroimage*. 2018;183:456–468.
45 Bookheimer SY, Salat DH, Terpstra M, et al. The lifespan human connectome project in aging: an overview. *Neuroimage*. 2019;185:335–348.
46 Van Essen DC, Smith SM, Barch DM, Behrens TEJ, Yacoub E, Ugurbil K. The Wu-minn human connectome project: an overview. *Neuroimage*. 2013;80:62–79.
47 Barisano G, Sheikh-Bahaei N, Law M, Toga AW, Sepehrband F. Body mass index, time of day and genetics affect perivascular spaces in the white matter. *J Cereb Blood Flow Metab*. 2021;41(7):1563–1578 [cited 2020 Nov 13]; Available from: http://journals.sagepub.com/doi/10.1177/0271678X20972856.
48 Lynch KM, Sepehrband F, Toga AW, Choupan J. Brain perivascular space imaging across the human lifespan. *Neuroimage*. 2023;271:120009 [cited 2023 Mar 13]; Available from: http://www.ncbi.nlm.nih.gov/pubmed/36907282.
49 Kim HG, Shin NY, Nam Y, et al. MRI-Visible dilated perivascular space in the brain by age: the human connectome project. *Radiology*. 2023;306(3). Available from: http://pubs.rsna.org/doi/10.1148/radiol.213254.
50 VanderWeele TJ. Principles of confounder selection. *Eur J Epidemiol*. 2019;34(3):211–219 [cited 2024 Sep 16]; Available from: https://pubmed.ncbi.nlm.nih.gov/30840181/.
51 van Buuren S, Groothuis-Oudshoorn K. Mice: multivariate imputation by chained equations in R. *J Stat Softw*. 2011;45(3):1–67 [cited 2024 Sep 20]; Available from: https://www.jstatsoft.org/index.php/jss/article/view/v045i03.
52 Inthout J, Ioannidis JP, Borm GF. The Hartung-Knapp-Sidik-Jonkman method for random effects meta-analysis is straightforward and considerably outperforms the standard DerSimonian-Laird method. *BMC Med Res Methodol*. 2014;14(1):1–12 [cited 2024 Sep 15]; Available from: https://bmcmedresmethodol.biomedcentral.com/articles/10.1186/1471-2288-14-25.
53 Schoenfeld D. Partial residuals for the proportional hazards regression model. *Biometrika*. 1982;69(1):239–241. https://doi.org/10.1093/biomet/69.1.239.
54 Durrleman S, Simon R. Flexible regression models with cubic splines. *Stat Med*. 1989;8(5):551–561 [cited 2023 Nov 11]; Available from: https://onlinelibrary.wiley.com/doi/full/10.1002/sim.4780080504.
55 Eilers PHC, Marx BD. Flexible smoothing with B-splines and penalties. *Statist Sci*. 1996;11(2):89–121. https://doi.org/10.1214/ss/1038425655 [cited 2024 Sep 16]; Available from: https://projecteuclid.org/journals/statistical-science/volume-11/issue-2/Flexible-smoothing-with-B-splines-and-penalties/10.1214/ss/1038425655.full.
56 Therneau TMT, Grambsch PM. *Modeling survival data: extending the Cox model*. New York, NY: Springer New York; 2000 (Statistics for Biology and Health). [cited 2023 Dec 16]. Available from: http://link.springer.com/10.1007/978-1-4757-3294-8.
57 Gray RJ. Flexible methods for analyzing survival data using splines, with applications to breast cancer prognosis. *J Am Stat Assoc*. 1992;87(420):942.
58 Hastie T. Pseudosplines. *J R Stat Soc Ser B*. 1996;58(2):379–396.
59 Box GEP, Tidwell PW. Transformation of the independent variables. *Technometrics*. 1962;4(4):531–550 [cited 2024 Sep 19]; Available from: https://www.tandfonline.com/action/journalInformation?journalCode=utch20.
60 Holm S. A simple sequentially rejective multiple test procedure. *Scand J Stat*. 1979;6(2):65–70. Available from: http://www.jstor.org/stable/4615733.
61 Schwarzer G, Carpenter JR, Rücker G. *Meta-Analysis with R*. Cham: Springer International Publishing; 2015 (Use R!). Available from: https://link.springer.com/10.1007/978-3-319-21416-0.
62 Bates D, Mächler M, Bolker BM, Walker SC. Fitting linear mixed-effects models using lme4. *J Stat Softw*. 2015;67(1):1–48 [cited 2023 Dec 16]; Available from: https://www.jstatsoft.org/index.php/jss/article/view/v067i01.
63 ggeffects Lüdecke D. Tidy data frames of marginal effects from regression models. *J Open Source Softw*. 2018;3(26):772 [cited 2023 Dec 16]; Available from: https://joss.theoj.org/papers/10.21105/joss.00772.
64 Iddi S, C Donohue M. Power and sample size for longitudinal models in R – the longpower package and shiny app. *R J*. 2022;14(1):264–282. Available from: https://journal.r-project.org/articles/RJ-2022-022.
65 Mowinckel AM, Vidal-Piñeiro D. Visualization of brain statistics with R packages ggseg and ggseg3d. *Adv Methods Pract Psychol Sci [Internet]*. 2020;3(4):466–483 [cited 2020 Dec 8]; Available from: http://journals.sagepub.com/doi/10.1177/2515245920928009.
66 Wickham H. *ggplot2*. Cham: Springer International Publishing; 2016 (Use R!). [cited 2023 Dec 16]. Available from: http://link.springer.com/10.1007/978-3-319-24277-4.
67 Mestre H, Tithof J, Du T, et al. Flow of cerebrospinal fluid is driven by arterial pulsations and is reduced in hypertension. *Nat Commun*. 2018;9(1):4878 [cited 2021 Aug 19]; Available from: https://www-nature-com.libproxy2.usc.edu/articles/s41467-018-07318-3.
68 Holstein-Rønsbo S, Gan Y, Giannetto MJ, et al. Glymphatic influx and clearance are accelerated by neurovascular coupling. *Nat Neurosci*. 2023;26(6):1042–1053 [cited 2023 Jun 8]; Available from: https://www-nature-com.stanford.idm.oclc.org/articles/s41593-023-01327-2.
69 Iliff JJ, Wang M, Liao Y, et al. A paravascular pathway facilitates CSF flow through the brain parenchyma and the clearance of interstitial solutes, including amyloid β. *Sci Transl Med*.

2012;4(147):1–11 [cited 2017 Sep 25]; Available from: https://www.science.org/doi/10.1126/scitranslmed.3003748.
70 Piantino J, Boespflug EL, Schwartz DL, et al. Characterization of MR imaging-visible perivascular spaces in the white matter of healthy adolescents at 3T. *Am J Neuroradiol*. 2020;41(11):2139–2145. https://doi.org/10.3174/ajnr.A6789.
71 Kim JY, Nam Y, Kim S, Shin NY, Kim HG. MRI-Visible perivascular spaces in the neonatal brain. *Radiology*. 2023;307(2).
72 Iliff JJ, Wang M, Zeppenfeld DM, et al. Cerebral arterial pulsation drives paravascular CSF-interstitial fluid exchange in the murine brain. *J Neurosci*. 2013;33(46):18190–18199 [cited 2017 Sep 25]; Available from: http://www.ncbi.nlm.nih.gov/pubmed/24227727.
73 Kress BT, Iliff JJ, Xia M, et al. Impairment of paravascular clearance pathways in the aging brain. *Ann Neurol*. 2014;76(6):845–861 [cited 2017 Sep 25]; Available from: http://www.ncbi.nlm.nih.gov/pubmed/25204284.
74 May C, Kaye JA, Atack JR, Schapiro MB, Friedland RP, Rapoport SI. Cerebrospinal fluid production is reduced in healthy aging. *Neurology*. 1990;40(3):500–503.
75 Hays CC, Zlatar ZZ, Wierenga CE. The utility of cerebral blood flow as a biomarker of preclinical alzheimer's disease. *Cell Mol Neurobiol*. 2016;36(2):167–179 [cited 2024 Jan 29]; Available from: https://link-springer-com.stanford.idm.oclc.org/article/10.1007/s10571-015-0261-z.
76 Duan W, Sehrawat P, Balachandrasekaran A, et al. Cerebral blood flow is associated with diagnostic class and cognitive decline in alzheimer's disease. *J Alzheimers Dis*. 2020;76(3):1103–1120.
77 Claassen JAHR, Thijssen DHJ, Panerai RB, Faraci FM. Regulation of cerebral blood flow in humans: physiology and clinical implications of autoregulation. *Physiol Rev*. 2021;101(4):1487–1559 [cited 2024 Jan 29]; Available from: https://pubmed-ncbi-nlm-nih-gov.stanford.idm.oclc.org/33769101/.
78 Schaeffer S, Iadecola C. Revisiting the neurovascular unit. *Nat Neurosci*. 2021;24(9):1198–1209 [cited 2021 Aug 7]; Available from: https://www-nature-com.libproxy2.usc.edu/articles/s41593-021-00904-7.
79 Wardlaw JM, Benveniste H, Nedergaard M, et al. Perivascular spaces in the brain: anatomy, physiology and pathology. *Nat Rev Neurol*. 2020;16(3):137–153 [cited 2020 Mar 24]; Available from: http://www.nature.com/articles/s41582-020-0312-z.
80 Hadaczek P, Yamashita Y, Mirek H, et al. The "perivascular pump" driven by arterial pulsation is a powerful mechanism for the distribution of therapeutic molecules within the brain. *Mol Ther*. 2006;14(1):69–78.
81 Rey J, Sarntinoranont M. Pulsatile flow drivers in brain parenchyma and perivascular spaces: a resistance network model study. *Fluids Barriers CNS*. 2018;15(1).
82 van Veluw SJ, Hou SS, Calvo-Rodriguez M, et al. Vasomotion as a driving force for paravascular clearance in the awake mouse brain. *Neuron*. 2020;105(3):549–561.e5 [cited 2022 Apr 13]; Available from: https://pubmed-ncbi-nlm-nih-gov.libproxy2.usc.edu/31810839/.
83 Smeijer D, Ikram MK, Hilal S. Enlarged perivascular spaces and dementia: a systematic review. *J Alzheimers Dis*. 2019;72(1):247–256 [cited 2023 Dec 1]; Available from: https://pubmed.ncbi.nlm.nih.gov/31561362/.
84 Rensma SP, van Sloten TT, Launer LJ, Stehouwer CDA. Cerebral small vessel disease and risk of incident stroke, dementia and depression, and all-cause mortality: a systematic review and meta-analysis. *Neurosci Biobehav Rev*. 2018;90:164–173 [cited 2023 Dec 1]; Available from: https://pubmed.ncbi.nlm.nih.gov/29656031/.
85 Zhu YC, Dufouil C, Soumaré A, Mazoyer B, Chabriat H, Tzourio C. High degree of dilated virchow-robin spaces on MRI is associated with increased risk of dementia. *J Alzheimer's Dis*. 2010;22(2):663–672 [cited 2017 Sep 25]; Available from: http://www.medra.org/servlet/aliasResolver?alias=iospress&doi=10.3233/JAD-2010-100378.
86 Romero JR, Pinheiro A, Aparicio HJ, DeCarli CS, Demissie S, Seshadri S. MRI-visible perivascular spaces and risk of incident dementia. *Neurology*. 2022;99(23):e2561–e2571 [cited 2023 Dec 1]; Available from: https://pubmed.ncbi.nlm.nih.gov/36175148/.
87 Xiong L, Boulouis G, Charidimou A, et al. Dementia incidence and predictors in cerebral amyloid angiopathy patients without intracerebral hemorrhage. *J Cereb Blood Flow Metab*. 2018;38(2):241–249. Available from: http://journals.sagepub.com/doi/10.1177/0271678X17700435.
88 Ding J, Sigurðsson S, Jónsson PV, et al. Large perivascular spaces visible on magnetic resonance imaging, cerebral small vessel disease progression, and risk of dementia. *JAMA Neurol*. 2017;74(9):1105 [cited 2023 Nov 30]; Available from: http://archneur.jamanetwork.com/article.aspx?doi=10.1001/jamaneurol.2017.1397.
89 Hernán MA. The hazards of hazard ratios. *Epidemiology*. 2010;21(1):13 [cited 2024 Sep 21];Available from: /pmc/articles/PMC3653612/.
90 Bouvy WH, Biessels GJ, Kuijf HJ, Kappelle LJ, Luijten PR, Zwanenburg JJM. Visualization of perivascular spaces and perforating arteries with 7 T magnetic resonance imaging. *Invest Radiol*. 2014;49(5):307–313 [cited 2017 Sep 25]; Available from: http://content.wkhealth.com/linkback/openurl?sid=WKPTLP:landingpage&an=00004424-201405000-00007.
91 Jochems ACC, Blair GW, Stringer MS, et al. Relationship between venules and perivascular spaces in sporadic small vessel diseases. *Stroke*. 2020;51(5):1503–1506 [cited 2020 Apr 16]; Available from: http://www.ncbi.nlm.nih.gov/pubmed/32264759.
92 George IC, Arrighi-Allisan A, Delman BN, Balchandani P, Horng S, Feldman R. A novel method to measure venular perivascular spaces in patients with MS on 7T MRI. *Am J Neuroradiol*. 2021;42(6):1069–1072 [cited 2021 Sep 3]; Available from: http://www.ajnr.org.libproxy2.usc.edu/content/early/2021/04/15/ajnr.A7144.
93 Oltmer J, Mattern H, Beck J, et al. Enlarged perivascular spaces in the basal ganglia are associated with arteries not veins. *J Cereb Blood Flow Metab [Internet]*. 2024;44(11):1362–1377 [cited 2024 Jul 29]; Available from: http://www.ncbi.nlm.nih.gov/pubmed/38863151.